Energy Storage Materials 71 (2024) 103566

Contents lists available at ScienceDirect

Energy Storage Materials

journal homepage: www.elsevier.com/locate/ensm

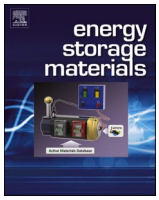

On the atomic structure of monolayer $V_4C_3T_z$ and the study of charge storage processes in an acidic electrolyte using SPEIS and *in-situ* X-ray absorption spectroscopy

Beatriz Mendoza-Sánchez [a,1,*], Atharva H. Ladole [a,b], Enrique Samperio-Niembro [a], Stefan Mangold [c], Michael Knapp [a], Eric N. Tseng [d], Per O.Å. Persson [d], Camille Douard [e,f], Christopher E. Shuck [g], Thierry Brousse [e,f]

[a] *Institute for Applied Materials-Energy Storage Systems (IAM-ESS), Karlsruhe Institute of Technology, Eggenstein-Leopoldshafen, D-76344, Germany*
[b] *Indian Institute of Science Education and Research, Dr. Homi Bhabha Road, Pashan, Pune, 411008, India*
[c] *Institute for Photon Science and Synchrotron Radiation, Karlsruhe Institute of Technology, Eggenstein-Leopoldshafen, D-76344, Germany*
[d] *Department of Physics, Chemistry and Biology, Linköping University,Linköping, SE-581 83, Sweden*
[e] *Nantes Université, CNRS, Institut des Matériaux de Nantes Jean Rouxel, IMN, 2 rue de la Houssinière BP32229, 44322 Nantes cedex 3, France*
[f] *Réseau sur le Stockage Electrochimique de l'Energie (RS2E), CNRS FR 3459, F-80039, France*
[g] *Department of Chemistry and Chemical Biology, Rutgers University, 123 Bevier Road, Piscataway, NJ 08854, USA*

ARTICLE INFO

Keywords:
$V_4C_3T_z$
MXene
Atomic structure
Monolayer
Supercapacitors
Charge storage processes
In situ XAS

ABSTRACT

Monolayer $V_4C_3T_z$ is synthesized and its atomic structure is studied using high-end transmission electron microscopy. X-Ray diffraction reveals key 3D to 2D crystal transformations as a V_4AlC_3 crystal is transformed into $V_4C_3T_z$ in synthesis processes. The charge storage properties of $V_4C_3T_z$ film electrodes are investigated for supercapacitor applications in 3 M H_2SO_4. $V_4C_3T_z$ film electrodes shows an excellent capacitance of up to 469.6 F g^{-1} and 845.7 F cm^{-3}, rate performance up to 30 A g^{-1} and cycling stability up to 10,000 cycles. A combination of electrochemical kinetics/mass transport models, staircase potentio-electrochemical impedance spectroscopy and *in situ* X-Ray absorption spectroscopy reveals, for the first time for this MXene, the underlying charge storage mechanisms, consisting of double layer capacitance, pseudocapacitance and a minor contribution from mass transport-controlled processes. The latter two implying a outstanding redox activity superior to Ti-based MXenes. The stability in standard environments, mechanical flexibility and the demonstrated excellent charge storage performance of $V_4C_3T_z$ makes it one of the best candidates for supercapacitor applications, especially in miniaturized devices.

1. Introduction

MXenes, $M_{n+1}X_nT_z$, are derived from $M_{n+1}AX_n$ precursors (termed MAX), where $n = 1–4$, *M* is an early transition metal (Ti, V, Mo, Ta, Nb, etc), A is an element of the group IIIA or IVA (e.g. Al, Ga, Si, Ge, etc), X is C and/or N and T_z describes surface chemical functionalities (–O, –F and –OH, –Cl groups and others) [1,2]. Other MXenes combining two M' and M'' transition metals, $(M'M'')_{n+1}X_nT_z$, have been theoretically predicted and/or experimentally obtained [3,4]. To date, more than 30 stoichiometric MXenes have been synthesized [2,5].

Amongst the outstanding applications of MXenes, energy storage is on the first line including applications in supercapacitors [6] and batteries [7–10]. A variety of properties make MXenes ideal for energy storage applications. First, as 2D nanomaterials, MXenes are all surface area available for capacitive energy storage [6]. Second, the transition metal M with a range of available oxidation states enables a rich redox activity [6,11,12]. Third, nanochannels (spaces in between nanosheets) are available for ion/solvent molecules intercalation [6,12–15]. MXenes have proved to store charge in a variety of aqueous [16] and organic electrolytes [7–9,17] consisting of mono and multivalent ions including Li^+, Na^+, K^+, Mg^{+2}, Al^{+3}. Lastly, physical properties such as high electrical conductivity [18] favor a fast electrical transport enabling a

* Corresponding author.
E-mail address: beatriz.sanchez.wa@gmail.com (B. Mendoza-Sánchez).
[1] First and Senior author.

https://doi.org/10.1016/j.ensm.2024.103566
Received 13 December 2023; Received in revised form 22 May 2024; Accepted 12 June 2024
Available online 11 July 2024

high-rate response of energy storage devices; and mechanical stability and flexibility make MXene-based electrodes attractive for applications in micro-/wearable electronics [6,19].

The rapidly growing MXene family offers an extraordinary variety of chemistries for deployment in energy storage. MXenes that have been applied in energy storage include Ti-based MXenes, $Ti_3C_2T_z$ [16], Ti_2CT_z [20,21], Mo-based MXenes, Mo_2CT_z [22], $Mo_{1.33}CT_z$ [23], V-based MXenes V_2CT_z [24,25], Mo/Ti-based MXenes $Mo_2TiC_2T_z$ [26] and Mo/V-based MXenes $Mo_xV_{4-x}C_3$ [27]. Energy storage performance is determined by the MXenes chemical and physical properties. This includes chemical composition, stoichiometry, degree and quality of delamination, presence of defects, chemical surface groups, and stability in application environments (atmosphere and electrolytes) against oxidation. Amongst all MXenes, V-based ones result attractive due to the several available valence states +2, +3, +4, +5 for redox activity. The first synthesized V-based MXene was V_2CT_z. V_2CT_z has been successfully applied in supercapacitors [24,25]. However, a well known marked instability of this MXene in standard atmospheres is a clear disadvantage for applications [28]. In 2008, V_4AlC_3 was synthesized for the first time [29], but only until recently the first attempts to synthesize the corresponding $V_4C_3T_z$ MXene using acid-based etching methods were made [30]. However, only multilayer, i.e. partially etched material, was reported in this work [30]. A delaminated MXene [14], generally, stores larger charge than a multilayer one [31,32] due to its intrinsic higher surface area and abundance of surface chemical groups involved in surface-based charge storage(Eq. (1)) [14]. Most studies to date in energy storage focus on multilayer rather than fully delaminated material [33–35]. Recently, the synthesis of fully delaminated $V_4C_3T_z$ has been achieved by us [36] and other authors [37,38]. However, the quality in terms of number of layers and crystal defects varies according to synthesis methods and protocols, which has an impact on electrical and charge storage properties. In this work, we emphasize the synthesis of $V_4C_3T_z$ in mono- to few-layers form. Importantly, we have found this material to be of far superior stability than V_2CT_z in standard atmospheres, both in suspension and in film form. In addition, as a 4:3 MXene, $V_4C_3T_z$ has a larger interlayer space available for ion intercalation (c lattice parameter of 30.3364 Å, here found) than MXenes with other stoichiometry such as 3:2, e.g. $Ti_3C_2T_z$(c lattice parameter of 20.6 Å [39]). Larger interlayer spaces may enable a multilayer ion-adsorption, implying higher capacity, of ions other than Li such as Na^+, K^+, Ca^{2+}, Mg^{2+} and Al^{3+} in battery set ups, as it has been theoretically predicted for Mg^{2+} for O-terminated Ti-, V- and Nb- based 3:2 and 2:1 MXenes [40].

Understanding of charge storage mechanisms of MXenes is key for the design of energy storage devices. To date in-depth studies of energy storage processes have been focused mainly on $Ti_3C_2T_z$. Particularly, in 1 M or 3 M H_2SO_4, $Ti_3C_2T_z$ delivers high energy energy density at high rates. The two main energy storage mechanisms in place have been proposed: electrical double layer capacitance (EDLC) and intercalation pseudocapacitance [12–15]. The latter implying ion intercalation processes within the MXene nanochannels and redox processes [12,13]. The redox processes involve –O chemical surface groups in $Ti_3C_2O_x$, electrons, and protons from the acidic electrolyte [14]:

$$Ti_3C_2O_x(OH)_yF_z + \delta e^- + \delta H^+ \rightarrow Ti_3C_2O_{x-\delta}(OH)_{y+\delta}F_z \quad (1)$$

where the reduction of the transition metal is mediated by protonation of the O atoms in a similar manner than in the case of the pseudocapacitive activity of RuO_2 [41,42]:

$$Ti_3^{n+}O_x^{2-}(OH^-)_y + \delta e^- + \delta H^+ \rightleftharpoons Ti_3^{[n+\ -(\delta/3)]}O_{x-\delta}^{2-}(OH^-)_{y+\delta} \quad (2)$$

where n + and [n + - (δ/3)] are the oxidation states of the Ti atom before and after reduction. Evidence of the protonation of -O groups under negative polarization has been provided by a combination of UV-*vis* and Raman spectroscopies [43].

On the other hand, experimental studies using X-ray absorption spectroscopy (XAS)[12] and electrochemical quartz crystal microbalance [13] have proved the redox activity of the Ti and the involvement of proton/cation intercalation within nanochannels in electrodes under negative polarization [13,44]. Ion intercalation was further confirmed by *in situ* XRD studies that revealed *c* lattice parameter expansion/contraction during electrochemical testing in 1 M H_2SO_4 [15]. Findings indicated a predominant intercalation pseudocapacitance mechanism at a − 0.7 to − 0.1 vs. Ag/AgCl potential range and a predominant EDLC mechanism at − 0.1 to 0.2 V vs. Ag/AgCl potential range [44].

Other studies give insights into the dynamics of proton transport and its correlation with storage processes. Rate limiting steps, such as proton intercalation in between nanochannels, have been recognized [44,45]. Findings indicate that water plays a key role on proton transport within nanochannels via the formation of dynamic proton-water networks, where 1 rather than 2–3 water layers favor faster redox processes [44,45]. The presence of –OH functional group was found to favor water intercalation during electrochemical cycling of electrodes, whereas an excess of –OH groups was found to disturb the proton-water networks hampering the proton transport [44]. In this work we use the following concepts: EDLC processes are surface-based and involve no diffusion control, pseudocapacitive processes involve faradaic charge transfer, are surface-based and involve no diffusion control, and processes that are controlled by mass transport, where a range of phenomena, including ion intercalation events, are rate-determining steps in overall charge storage processes.

Herein, we have synthesized fully delaminated $V_4C_3T_z$, consisting of monolayer and few-layers material. The atomic structure of monolayer $V_4C_3T_z$ has been studied using high-end transmission electron microscopy. Aberration corrected high angle annular dark field scanning transmission electron microscopy (HAADF-STEM) revealed the atomic structural details of $V_4C_3T_z$ monolayer crystals, which is amongst the first MXenes with a 4:3 M:X stoichiometry studied at the atomic level [26]. Electron energy loss spectroscopy (EELS) and energy dispersive X-ray spectroscopy (EDX) confirmed the presence of V and C and surface chemical groups. X-ray diffraction (XRD) revealed key 3D to 2D crystal transformations as a V_4AlC_3 crystal is transformed into $V_4C_3T_z$ during synthesis. The energy storage properties of $V_4C_3T_z$ electrode films were investigated for applications in supercapacitors in a 3 M H_2SO_4 electrolyte. An outstanding high capacitance and capacity per unit mass and volume were revealed as well as an excellent rate performance and cycling stability. For the first time, the underlying charge storage processes of $V_4C_3T_z$ in 3 M H_2SO_4 were investigated using a key combination of methods: *in situ* XAS, cyclic voltammetry combined with electrochemical kinetics/mass transport models and staircase potentio-electrochemical impedance spectroscopy (SPEIS). Particularly, *in situ* XAS is a powerful tool that allowed us to identify and quantify, for the first time, the underlying redox processes over the full working electrochemical window. The combination of the three methods allowed to establish charge storage mechanisms at defined potential regions. Findings include an outstanding redox activity of V atoms surpassing the redox activity of Ti in Ti-based MXenes.

2. Experimental methods

2.1. Chemicals

Hydrofluoric acid, HF (48 wt.%, 27.58 M), hydrochloric acid HCl (37 wt.%, 12.17 M), tetrabutylammonium hydroxide, TBAOH (40 wt.% in water), were acquired from *Sigma Aldrich*, Germany. Deionized water (DI) of 18.2 MΩ cm resistivity was used for synthesis procedures.

2.2. Synthesis of V_4AlC_3

Vanadium powder (99.5 %, − 325 mesh, Alfa Aesar), aluminum powder (99.5 %, − 325 mesh, Alfa Aesar), and graphite (99 %, − 325

mesh, Alfa Aesar), were mixed in a 4:1.5:3 atomic ratio (10 g in total). The precursors were balled milled with 5 mm Yttria Stabilized Zirconia balls (2:1 ball:powder ratio) in plastic jars at 60 rpm for 18 h. The powder mixture was then transferred to alumina crucibles, which were placed into a high temperature tube furnace (*Carbolite Gero*). Ultra-high purity Ar (99.999 %) gas was continually flown (200 cm^{-3} min^{-1}) through the furnace for 1 h prior to heating and during the entire annealing procedure. The furnace was heated to 1500 °C at 3 °C min^{-1}, held for 2 h, then cooled to room temperature at 3 °C min^{-1}. The resulting solid block product was milled using a drill press with a TiN-coated milling bit. The powders were then sieved through a 400 mesh sieve, producing powders with a particle size < 38 μm. The powders were then washed with HCl 37 wt.%; 10 g of powder were added slowly to 20 ml of HCl 37 wt.% and stirred overnight. Then the acid was removed by vacuum-assisted filtration while flushing water until the filtrated liquid had pH = 7. The powders were then dried in vacuum at room temperature.

2.3. Synthesis of etched V_4AlC_3

Prior to etching procedures, particle size selection was performed. Powder of particle size < 36 μm was selected (using a 36 μm sieve) for etching processes. For the etching reaction a 50 ml polytetrafluoroethylene (PTFE) reaction vessel and magnetic stir bar were used. A HF (12 ml): HCl (12 ml): H_2O (6 ml), for a total of 30 ml, acid mix was carefully placed in the reaction vessel. Then, 1 g of V_4AlC_3 was added in small portions over 20 min while stirring at 50 rpm. The reaction vessel was then closed with the screw top lid giving 70 % of the turns necessary to fully close (important to allow gas evolution). The reaction vessel was then immersed in an silicon oil bath maintained at 45 °C with the level of oil up to the height of the reaction mix and magnetic stirring was set to 400 rpm. The reaction was performed for 7 d.

After etching, the reaction mixture was placed in conical centrifuge tubes (150 ml), DI water was added and centrifugation was done at 5000 rpm for 10 min. The acidic supernatant was collected with a pipette and discarded. This step was repeated until the supernatant reached pH 5–6. The etched powder was then further washed and collected by vacuum-assisted filtration, using PVDF membrane filters (0.22 μm pore size). DI water (500 ml) was continuously flushed, then the powders were left to settle and dry over the membrane filter (for 3–5 min) prior to collection.

2.4. Delamination of etched V_4AlC_3

For delamination, the etched powder was added to 10 wt.% TBAOH, in a 2:1 mol ratio of TBAOH:$V_4C_3T_z$, and stirred at 350 rpm, at 35 °C, for 17 h. Afterward, washing steps were carried out to retrieve the TBAOH. The TBAOH intercalated products were placed in conical centrifuge tubes (150 ml), DI water was added and centrifugation was done at 5000 rpm for 10 min. The top 70–80 % volume was pipetted out. This step was repeated until achieving pH 7–8, usually 3 steps. Then, DI water was added, the product was vigorously shaken by hand for 10 min, followed by centrifugation at 3500 rpm for 30 min. The top 70 % volume was pipetted out and constituted the delaminated material. This step was repeated 3 times to obtain more fractions of delaminated product. The $V_4C_3T_z/H_2O$ suspensions of delaminated material were either immediately processed for film manufacture or stored. Storing of $V_4C_3T_z/H_2O$ suspensions was done in gas-washing bottles bubbling with Ar for 5 min, followed by closing under Ar pressure and stored at 5 °C.

2.5. $V_4C_3T_z$ film manufacture

Delaminated films were manufactured using vacuum-assisted filtration. A standard glass vacuum filtration system and a *Celgard 3501* filter membrane (64 nm pore size) were used. To determine the suspension volume to filter to achieve a determined film thickness, calibration was necessary according to the concentration of the suspension. In general, to reduce concentration and facilitate a faster filtration, as-produced suspensions were purified by a centrifugation step at 5000 rpm for 30 min and collection of the top 70 % volume. In general, films were obtained by filtering 20–30 ml of $V_4C_3T_z/H_2O$ purified suspension per film. The film/filter membrane stack were then collected and dried in a *B-585* Büchi glass vacuum oven at room temperature for 5 h. The film was then separated from the membrane filter and the weight and thickness were measured. The film here used had a thickness of 8 μm. Electrodes used for electrochemical testing had a 3 mm diameter and a mass of i.e. 0.181 mg. Generally, the films were stored in a glove box (< 0.1 ppm O_2, < 0.1 ppm H_2O).

2.6. Equipment

Centrifugation was performed using a centrifuge (Thermo Scientific Heraeus Multifuge X1R) equipped with a TX-400 rotor (16.8 cm radius). The relative centrifugal force (RCF), measured in gravity accelerations (*g*) units, is defined as

$$RCF = 1.118 \times 10^{-5} S^2 \times r \quad (3)$$

where S is the centrifugal rotational speed (rpm), and r is the radius of the rotor (cm). This formula should be used to convert the S cited in this work to RCF. The mass of the powders was measured using a balance (Sartorius, Germany) with a 0.0001 g readability and a ± 0.00015 g accuracy. The mass of electrodes was measured using an ultra-microbalance (Mettler Toledo XPR2U) with a 0.0001 mg readability and a ± 0.00015 mg accuracy. The thickness of film electrodes was measured with a *HEIDENHAIN ND280* length gauge with a 0.0001 mm readability.

2.7. Materials characterization methods

Scanning electron microscopy (SEM) was performed in a *ZEISS Merlin* (*ZEISS*, Germany) microscope equipped with a GEMINI II column and using the *In Lens* detector. Energy dispersive X-ray spectroscopy (EDX) was acquired using a *Quantax* detector at 15 keV energy.

Standard and high-resolution high angle annular dark field scanning transmission electron microscopy (HAADF-STEM) imaging and electron energy loss spectroscopy (EELS) were used to obtain structural and elemental analysis at the atomic level. The microscopy was performed using a double C_s corrected *FEI Titan*^{3} *60–300* (Linköping, Sweden), operated at 300 kV. EELS was performed using the embedded *Gatan* imaging filter (GIF) *Quantum ERS* and spectra were acquired using the *Digital Micrograph* software, and processed using built-in functions.

The $V_4C_3T_z/H_2O$ sample was drop-casted onto Lacey Carbon Cu TEM grids, mounted in a double-tilt holder and dried at high vacuum conditions and at room temperature overnight using a high vacuum chamber. Specimen contamination was reduced by performing an electron beam flooding (beam shower) with a beam current of 100 pA for 1 h prior to imaging. HAADF-STEM images were simulated using the *Dr. Probe* software, using a V_4C_3 crystal supercell and specific imaging conditions of the experimental session. The supercell was built from a corresponding V_4C_3 crystallographic information file (CIF) using *CrystalMaker* software. Diffraction patterns were obtained from Fast Fourier Transform (FFT) operations of STEM images, using the *Digital Micrograph* software. Simulated diffraction patterns were obtained using the V_4C_3 CIF and *CrystalMaker* software.

X-ray diffraction (XRD) was performed in a *STOE STADI P* diffractometer with a Mo Kα1 radiation source ($\lambda = 0.7093$ Å, 50 kV, 40 mA), a Ge 111 monochromator and a MYTHEN 1D silicon strip detector. The samples were measured using a *Debye-Scherrer* geometry using glass capillaries (No. 50, 0.5 mm diameter, 0.01 mm thickness). The data was acquired from $2\theta = 2$ to 92 ° in $2\theta = 0.495$ ° steps and acquisition of 1.98 min/step for a total measuring time of 6 h. Each measurement was done twice to ensure reproducibility. XRD was analyzed using *FullProf*

software package [46].

In situ X-ray absorption spectroscopy (XAS) was performed at the XAS beamline of the KIT synchrotron, which uses three ionization chambers *IC Spec* chamber (*FMB-Oxford*). Pristine $V_4C_3T_z$ films and V, V_2O_3, VO_2, V_2O_5 reference compounds were also measured. All the measurements were done in transmission mode. The pristine films and reference compounds were measured using one of the ionization chambers and a double crystal monochromator using a Si 111 crystal pair. Such samples were measured inside a vacuum chamber to maximize the signal-to-noise ratio and to reduce sample changes induced by the beam. A dedicated holder was used for mounting and transferring the samples. The *in situ* measurements were performed using a customized cell (described in the Electrochemical Methods section), which was placed between the second and third ionization chambers.

For the measurements, the position (energy) of the V-K absorption edge was determined via the maximum in the first derivative of the spectrum of a V foil measured in parallel. The *in situ* measurements and the measurements of the reference compounds were done in a continuous scanning mode starting at 150 eV before the edge position and ending at 800 eV after the edge position with a time per scan of 260 s. The measurements of the pristine films were done in a step mode.

2.8. Electrochemical methods

Electrochemical cell. Electrochemical tests were run in 1/4 inch 3-electrode perfluoroalkoxy alkane (PFA) *Swagelok* cells using 6 mm diameter glassy carbon rods as current collectors. Half-cell tests were performed using disc electrodes of $V_4C_3T_z$ film as working electrode (3 mm diameter, thickness of 8 μm, a mass of i.e. 0.181 mg), an overcapacitive carbon film as counter electrode (5 mm diameter), an Ag/AgCl reference electrode and a *Celgard 3501* film (6 mm diameter) as separator. The electrolyte used was 3 M H_2SO_4. The electrolyte was degassed using nitrogen bubbling for 2–3 min before electrochemical tests. Full cells tests were performed using $V_4C_3T_z$ films as negative electrode, a carbon film as positive electrode and the same electrolyte. The full cell was tested in a 1.35 V electrochemical window. Details of balance of mass of positive and negative electrodes are given in the Supporting Information (Section S7).

***In situ* electrochemical cell for XAS measurements.** An *in situ* cell was built and customized for XAS measurements in transmission mode [47,48]. The cell is a "beaker" type cell suited for a 3-electrode set up with three compartments for working, counter and reference electrodes. Two glassy carbon plates were used as current collectors. The plates had an opened area for beam transmission. The $V_4C_3T_z$ film was placed and fixed in between the current collectors. A graphite rod was used as counter electrode and a Ag/AgCl electrode was used as reference. The electrolyte used was 3 M H_2SO_4.

Manufacture of the overcapacitive carbon electrode. Overcapacitive carbon film electrodes had a mass composition of: *YP-50 Kuraray* activated carbon (75 wt.%), *C65* conductive carbon (15 wt.%) and PTFE (10 wt.%). Manufacture of the carbon film electrode was done by mixing, using a *THINKY ARV-310* planetary vacuum mixer, and manual rolling with the aid of a table/rod set. The carbon mix was placed in a recipient, 2–3 ml of ethanol/isopropanol (1:1 V/V ratio) were added and mixing was done at 1500 rpm x 10 min x 5 times until a slurry was achieved. Then, the PTFE was added and mixing was done at 1500 rpm x 5 min x 3 times until a paste-like consistence was achieved. Afterward, the paste was placed in between plastic foils and a film was manufactured by consecutive manual rolling-folding steps until the desired thickness was achieved (typically 600 μm to 1 mm). The film was dried at 80 °C for 1 h in a standard atmosphere oven.

Electrochemical tests. Electrochemical tests were run in an *VMP300* (*BioLogic*) potentiostat using *EC-Lab* software. Cyclic voltammetry (CV) was run from $V_1 = -0.35$ V to $V_2 = 0.4$ V *vs.* Ag/AgCl potential window limits at 0.5 to 500 mV s^{-1} scan rates. The capacitance *C* (F) was calculated as

$$C^{+/-} = \frac{\Delta Q^{+/-}}{\Delta V} = \frac{\int I^{+/-}(V)dt}{(V_2 - V_1)} \quad (4)$$

where anodic (+) and cathodic (-) charge $Q^{+/-}$ (C) were obtained by numerical integration of the corresponding $I^{+/-}$ currents of the cyclic voltammogram (CV). V_1 and V_2 (V) are the potential window limits of the CV and *t* (s) is time. The Coulombic efficiency (CE) was calculated as (Q^+/Q^-) x 100.

Galvanostatic cycling with potential limitation (GCPL) was performed from $V_1 = -0.35$ V to $V_2 = 0.4$ V *vs.* Ag/AgCl potential window and at 0.25 to 30 A g^{-1} for rate performance tests and at 10 A g^{-1} for cycling tests. The CE was calculated as ($Q_{charge}/Q_{discharge}$) x 100. The cycling stability tests were performed over 10,000 cycles, in sets of 2,000 cycles. When necessary, the electrolyte was topped up every 2,000 cycles.

Staircase potentio-electrochemical impedance spectroscopy (SPEIS), a technique suitable to perform successive electrochemical impedance spectroscopy (EIS) measurements during a potential scan, was used to study electrochemical kinetics [49–51]. SPEIS was used along a CV scan in an open circuit potential (OCP) to V_1 to V_2 to OCP sequence. Polarization (holding DC potential) was done every 25 mV during 10 min before the performance of each EIS measurement. EIS was performed by applying a single sine alternate voltage of 10 mV amplitude ($V_{rms} = 7.07$ mV). Measurements were done in a 4 mHz to 250 kHz frequency range, reading 10 points per decade (logarithmic scale) and averaging 5 measurements per read frequency point. A waiting period of $p_w = 0.1$ (1/frequency) (s) was set before reading each frequency point.

The capacitance *C (ω)* of the half-cell was calculated from the impedance data modeling the total impedance of the system *Z* as the impedance of a capacitor [52]:

$$Z = \frac{1}{j\omega C(\omega)} \quad (5)$$

where $\omega = 2\pi f$ is the angular frequency with $f =$ frequency (Hz); $j = \sqrt{-1}$. Considering impedance in its complex form Z = Z' + jZ", the real component of the capacitance *C' (ω)* can be calculated as:

$$C'(\omega) = \frac{-Z''(\omega)}{\omega|Z(\omega)|^2}, \quad (6)$$

and the imaginary component of the capacitance C"(ω) can be calculated as:

$$C''(\omega) = \frac{Z'(\omega)}{\omega|Z(\omega)|^2} \quad (7)$$

where $|Z(\omega)|$ is the magnitude of the impedance. The phase angle ϕ is calculated as

$$\phi = -\tan^{-1}\frac{Z'(\omega)}{Z''(\omega)} \quad (8)$$

Electrochemical tests for the *in situ* XAS studies. XAS was measured during potentiostatic steps at defined potentials of interest within a $V_1 = -0.35$ V to $V_2 = 0.4$ V *vs.* Ag/AgCl electrochemical window. Namely at 0.345 V (OCP), 0.2 V, 0.05 V, − 0.1 V, − 0.25 V, − 0.35 V in reduction and at − 0.322 V, − 0.2 V, − 0.05 V, 0.05 V, 0.15 V, 0.25 V and 0.4 V in oxidation. Potentiodynamic steps were performed at 10 mV s^{-1} to advance in between the potentiostatic steps of interest. Two cycles were measured and a last potentiostatic step was at 0.345 V (OCP). The potentiostatic steps were set for 15 min and 10 s, which allowed for the acquisition of 3 XAS spectra per potential of interest. Only the last 2 XAS spectra were taken into account for oxidation/reduction states calculation. In addition a set of a 3 x 3 additional spectra were acquired without polarization.

3. Results and discussion

The material was synthesized according to procedures described in the experimental section. The key steps are described here (Scheme 1). The Al of the precursor V_4AlC_3 (Scheme 1a) is etched away using a HF/HCl/H_2O mix at 45 °C for 7 d (Scheme 1b). The product is a multilayer material, which generally, retains some Al atoms in composition and, in the case, of V-based MXenes, V is, to some degree, also etched away [53]. Thus, rendering a compound of the following composition: $V_{4-x}Al_{1-y}C_3T_z$, where *x* and *y* account for V and Al atoms that had been etched away and T_z are surface chemical functionalities, expected to be -O, -OH,-F and -Cl, as per the generality of MXenes synthesized under these conditions (Scheme 1c). Subproducts of the reaction include $[AlF_n]^{(3-n)}$ species, including AlF_3(aq) [53]. The related reaction mechanisms have been largely discussed in our previous work [53]. Subsequently, the multilayer material is delaminated using ion exchange intercalation, where H^+ are exchanged by TBA^+ ions(Scheme 1d-e). The final product consist of $V_{4-x}C_3T_z$ flakes (Scheme 1e).

3.1. Microscopy studies

HAADF-STEM imaging was performed to explore the morphology and atomic structure of the obtained $V_4C_3T_z$ flakes and to confirm the successful delamination of monolayer $V_4C_3T_z$ flakes (Fig. 2a). The flake size (largest dimension) was obtained from the observation and measurement of multiple flakes with dimensions ranging from ≈ 200 nm to 2.0 μm. Representative flakes are shown in Fig. 2a. To verify that the observed flakes were monolayer nanosheets, the thickness was measured using HAADF-STEM intensity profiles and EELS (Fig. 2b-c). The procedure for thickness determination is described in our previous work (Supporting Information, section S7 [54]). The measured thickness across the thinnest flakes was ≈ 1.5 nm (Fig. 2), which, according to the cell parameters measured by XRD below (c = 30.3364 Å, d space of 15.1682 Å), corresponded to a monolayer nanosheet. For reciprocal space comparison, a fast Fourier transform (FFT) of the high resolution image (in Fig. 2d) was produced and indexed (Fig. 2g). The FFT matches the simulated diffraction pattern of a single layer crystal (Fig. 2h), confirming the single layer nature of the obtained material.

High resolution images revealed the atomic structure of the $V_4C_3T_z$ nanosheets (Fig. 2d). The images showed a weak densely close-packed atom lattice, superimposed with a more intense but sparsely close-packed lattice. This structure was explained with aid of a simulated atomic model and corresponding simulated image (Fig. 2e). In the atomic structure of the $V_4C_3T_z$, at a column of atoms 1, the top and bottom V layers overlap (cross-sectional view [100], Fig. 2e bottom) resulting in stronger mass contrast, i.e., the brighter yellow spots in the plan-view [001], (Fig. 2e top). Conversely, at the other atom columns 2 and 3, only one V atom is present (Fig. 2e bottom), resulting in a comparatively weaker mass contrast, i.e., the dimmer spots in the plan-view image (Fig. 2e top). The atom columns 1 repeat periodically every fourth atoms along the y-axis (Fig. 2e). The experimentally obtained image matches the simulated image (Fig. 2d) and atomic model (Fig. 2e) and confirms the structure of the nanosheets.

In addition to the pristine structure, vacancies on V sites are identified (local dark spots) (Fig. 2d). Moreover, a few surface adatoms can be observed (bright spots). Since they are brighter than V atoms, these adatoms must correspond to a heavier element, most likely originated from synthesis residues. The HAADF-STEM images also revealed the presence of pores that were approximately 3 nm wide (Fig. 2f). The presence of pores is highly desired to promote ion transport across nanosheets in the energy storage applications here pursued [14].

EELS was performed to study elemental composition. EELS confirmed the presence of V and C in the nanosheets (Figure S1a). The presence of O as a surface chemical group is difficult to assess from the EELS spectra (Figure S1a). Besides a poor signal to noise ratio, the main reason for this is the overlap between the large cross-section of the V $L_{3,2}$-edge and the comparatively smaller cross-section of the O K-edge. An extended acquisition from a single sheet was performed (Figure S1b). The onset of the O K-edge is on the declining signal slope of V-L_2, making it challenging to separate the two signals. However, there is an apparent signal at approximately 537 eV energy loss, which is identified as part of the O K-edge (Figure S1b). Previous work on EELS of vanadium oxides, where the O:V mol ratio was much higher than here, e.g. 3/2 for V_2O_3, show that the O K-edge is just visible as superimposed on the V edge [55]. Assuming that for the present MXene, all the surface chemical groups would be O, then the O:V ratio would be 1:2 and the corresponding O K-edge would be barely visible. Accordingly, we identify O to be present as a surface chemical group, but with a signal that is too weak to quantify. Supporting these studies, EDX confirmed the presence of V, C, O and also F and Cl, which could not be detected by EELS (Figure S2).

An electrode film manufactured by vacuum filtration is shown in

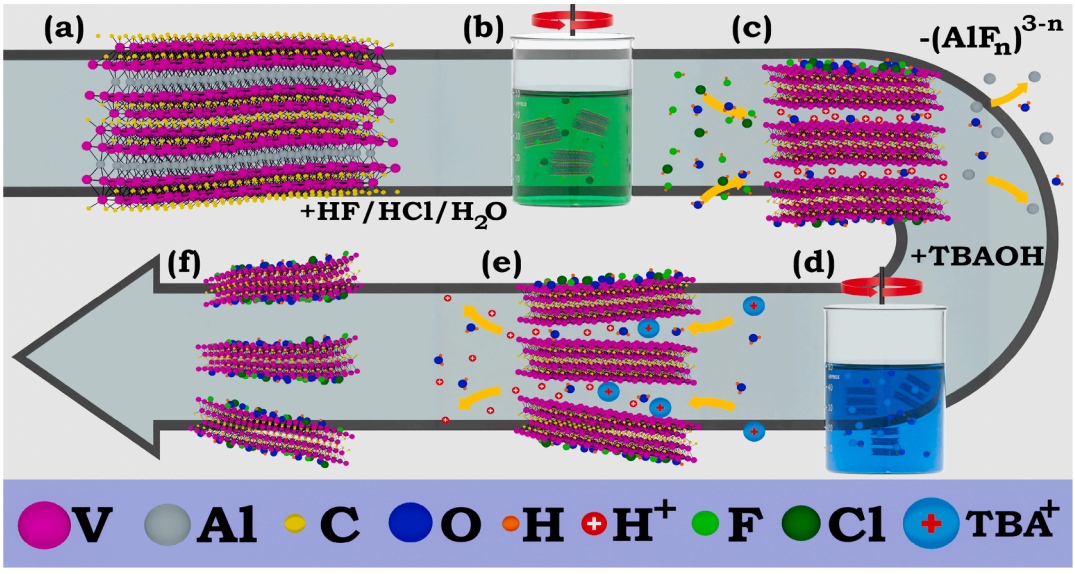

Fig. 1. Synthesis procedure: (a) V_4AlC_3 and an acid mix are combined in an (b) etching reaction to yield (c) multilayer $V_{4-x}Al_{1-y}C_3T_z$ and subproducts, (d) the multilayer material is then combined with TBAOH in a delamination step where (d) H^+ are exchanged with TBA^+ ions to deliver (e) $V_{4-x}C_3T_z$ delaminated flakes.

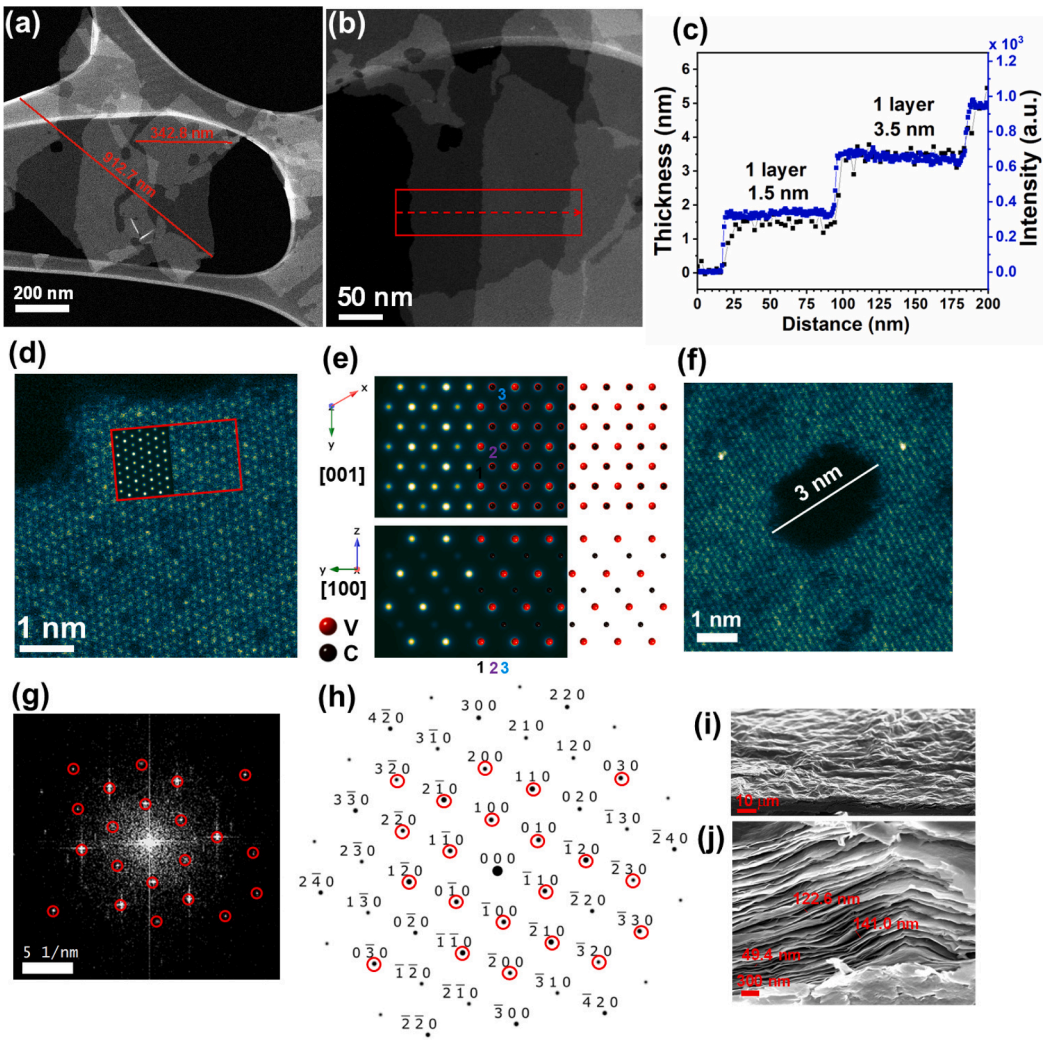

Fig. 2. (a) HAADF-STEM image of $V_4C_3T_z$ flakes with lateral size indicated, (b) HAADF-STEM image of several overlapping $V_4C_3T_z$ flakes, indicating a region of interest for measurements of (c) intensity profiles (showing incremental contrast steps) and thickness profiles determined by EELS, (d) HAADF-STEM image of a $V_4C_3T_z$ with an overlaid (e) simulated atomic structure image (left) and a V_4C_3 atomic model (right) showing a plan-view [001] (top) and cross-sectional view [100] (bottom) of the crystal - numbers indicate atom columns -, (f) HAADF-STEM image of a $V_4C_3T_z$ flake showing a pore, (g) FFT of a $V_4C_3T_z$ crystal lattice and (h) indexation according to a simulated diffraction pattern of a V_4C_3 crystal, (i-j) SEM images of a $V_4C_3T_z$ film obtained by vacuum filtration.

Fig. 2i-j. The thickness of this film was 6.8–9 μm. Fig. 2i shows a 6.9 μm section of this film and Fig. 2j a close up of the top 3 μm. The as-manufactured films were wavy (top view Fig. 2i) and showed nano-channels (spaces in between stacks of nanosheets) of size up to 141 nm (Fig. 2j), which facilitated electrolyte infiltration.

3.2. XRD analysis

The crystal structure of V_4AlC_3 was studied. Rietveld refinement (RR) confirmed the presence of V_4AlC_3 as the main phase and several minor secondary phases (Fig. 3). The crystal structure and structural parameters are reported in Table 1. Crystallographic information files were obtained from data basis (indicated in Table 1), except for V_4AlC_3, for which crystallographic information was generated using our own raw data and general guidance from previous reports [29]. Further details of the Rietveld Refinement are given in the Supporting Information, Section S3.

Several secondary phases were found. Evidence of phases VC and V_6C_5 were reflections of minor intensity or shoulders, most likely describing crystals that inherently grew with V_4AlC_3. Then, few low intensity reflections described phases V_2O_5 and Al_2O_3. The former is expected as per the reactivity of vanadium in standard atmospheres. Al_2O_3 is attributed to residuals from crucibles used in the synthesis. Importantly, no V_2AlC phase was found, which is highly undesirable for the synthesis and analysis of the target $V_4C_3T_z$ MXene [39,53].

Etched and delaminated samples were studied by XRD. A comparative analysis versus the precursor V_4AlC_3 revealed key structural changes (Fig. 4). The etched sample was composed of two main phases: unetched V_4AlC_3 and the etched $V_{4-x}Al_{1-y}C_3T_z$ [53]. In the following analysis, three 2θ regions were considered.

At $2\theta = 1$–10° angles, V_4AlC_3 showed 00l reflections (due to basal planes). Upon etching and delamination, the 002, 004 and 008 shifted to lower 2θ angles, which indicated an increasing expansion of the c lattice parameter (Fig. 4a,b). As calculated from the 2θ angles of the 002 reflection, the c lattice parameters were: 29.6451 Å (d space of 14.8225 Å) for the etched sample and 30.3364 Å (d space of 15.1682 Å) for the delaminated sample. Broadening of the 00l reflections, upon etching and even further upon delamination indicated a transition from a 3D V_4AlC_3 crystal to 3D multilayer and to 2D crystals of the etched and delaminated products, respectively. For the limit of monolayer material, the 002 reflection is expected to vanish [56]. However, the sample tested consisted of milled pieces of a film obtained by vacuum filtration (mounted in a capillary and measured in transmission mode) where delaminated crystals are expected to re-stack along the c axis with a degree of rotation

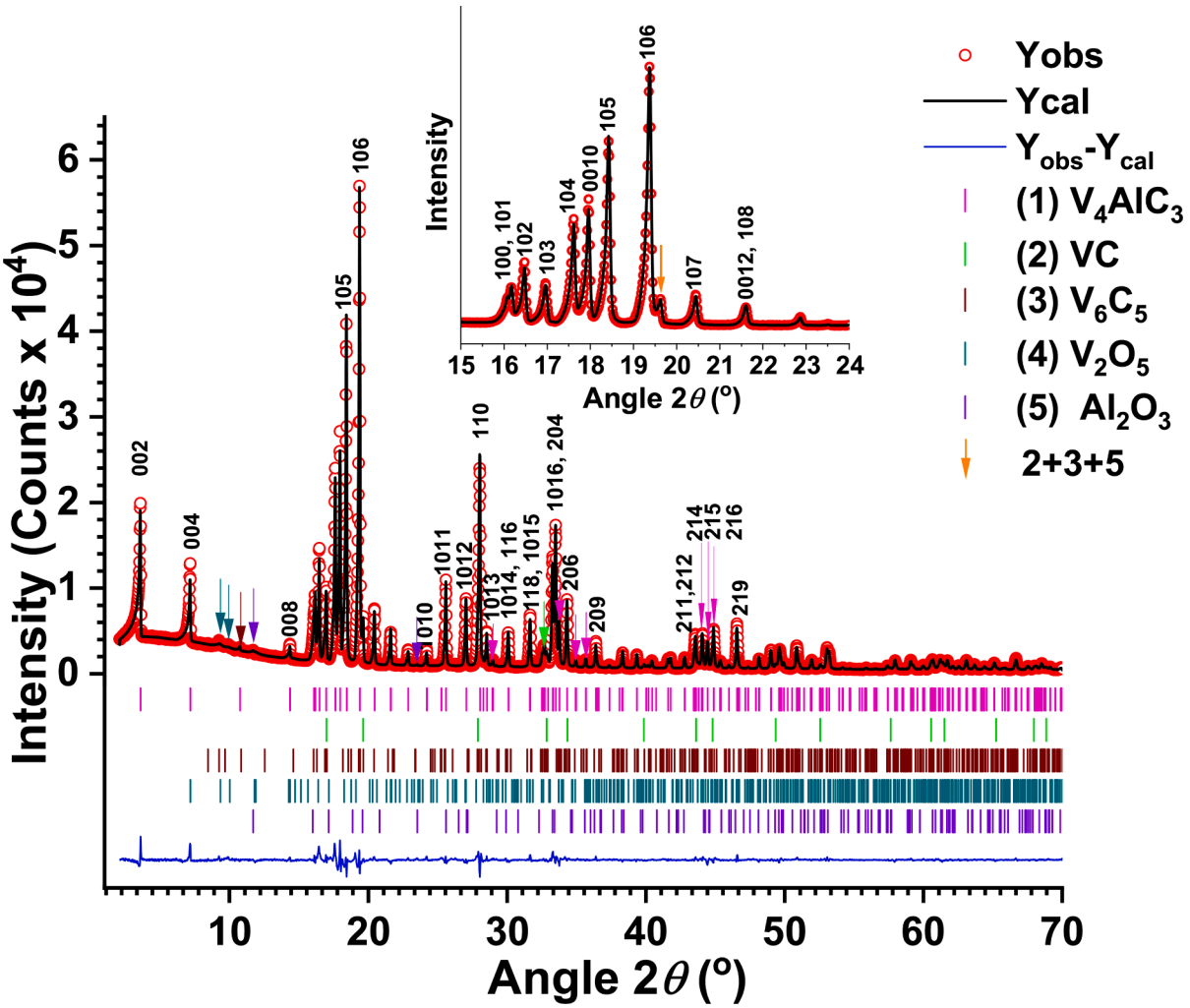

Fig. 3. XRD pattern of V_4AlC_3 and calculated model from Rietveld refinement.

Table 1
Structural parameters of phases in V_4AlC_3. Numbers in brackets give statistical deviations for the digit to the left. Standard deviations have been multiplied by the Bérar factor to correct for local correlations. The profile R-factor $R_p = 4.08$, the weight profile R-factor $R_{wp} = 5.5$ and $\chi^2 = 6.53$.

Phase	Space group (source)	a (Å)	b (Å)	c (Å)	$\alpha = \beta$ (°)	γ(°)	wt.%
V_4AlC_3	P 6_3/m m c	2.92795(6)	2.92795(6)	22.7116(5)	90	120	91.85(0.51)
VC	F m − 3 m (ICSD 22263)	4.1622(3)6	4.1622(3)6	4.1622(3)6	90	90	2.55(0.17)
V_6C_5	P 31 1 2 (ICSD 71098)	5.083(1)16	5.083(1)16	14.471(5)49	90	120	1.48(0.03)
V_2O_5	P m n 21 (ICSD 1011126)	11.36(7)953	4.35(2)314	3.59(2)738	90	90	3.13(0.37)
Al_2O_3	R − 3 c (ICSD 9770)	4.760(3)86	4.760(3)86	12.98(2)990	90	120	0.99(0.18)

and shift respect to each other. Previous studies in other 2D nanomaterials showed that the 002 reflection of crystals of at least 2 layers is insensitive to interlayer rotation around the c axis and shift respect to each other [56]. Thus, the 002 peak can be well explained by a re-stacking of delaminated monolayers with a degree of interlayer disorder. A fraction of few-layers crystals also contribute, which were also detected by TEM ((Figure S1).

At 2θ = 15.6–23.5 ° angles, V_4AlC_3 showed mostly h0l reflections, the 100 reflection, and the 0010 reflection (Fig. 4c). Upon etching, the h0l and 100 reflections showed a decrease in intensity and broadening, both indicating a 3D to 2D crystal transformation. In most cases, these reflection seemed to have also shifted to higher 2θ angles. For instance, reflections 1 and 2 (etched sample), could be 101 and 102 reflections (V_4AlC_3) shifted to higher 2θ angles. The same could be said for reflections 4 and 5 (etched sample), with respect to 105 and 106 reflections (V_4AlC_3), respectively. Although reflection 5, could well be the pervasive presence of secondary phases, even upon etching. In contrast, reflection 6 (etched sample) could be the reflection 108 (V_4AlC_3) shifted to lower 2θ angles.

Upon etching interlayer crystal disorder is expected. Previous studies in other 2D nanomaterials establish that h0l reflections are sensitive to the number of layers and interlayer ordering [56]. As the limit of 1 layer

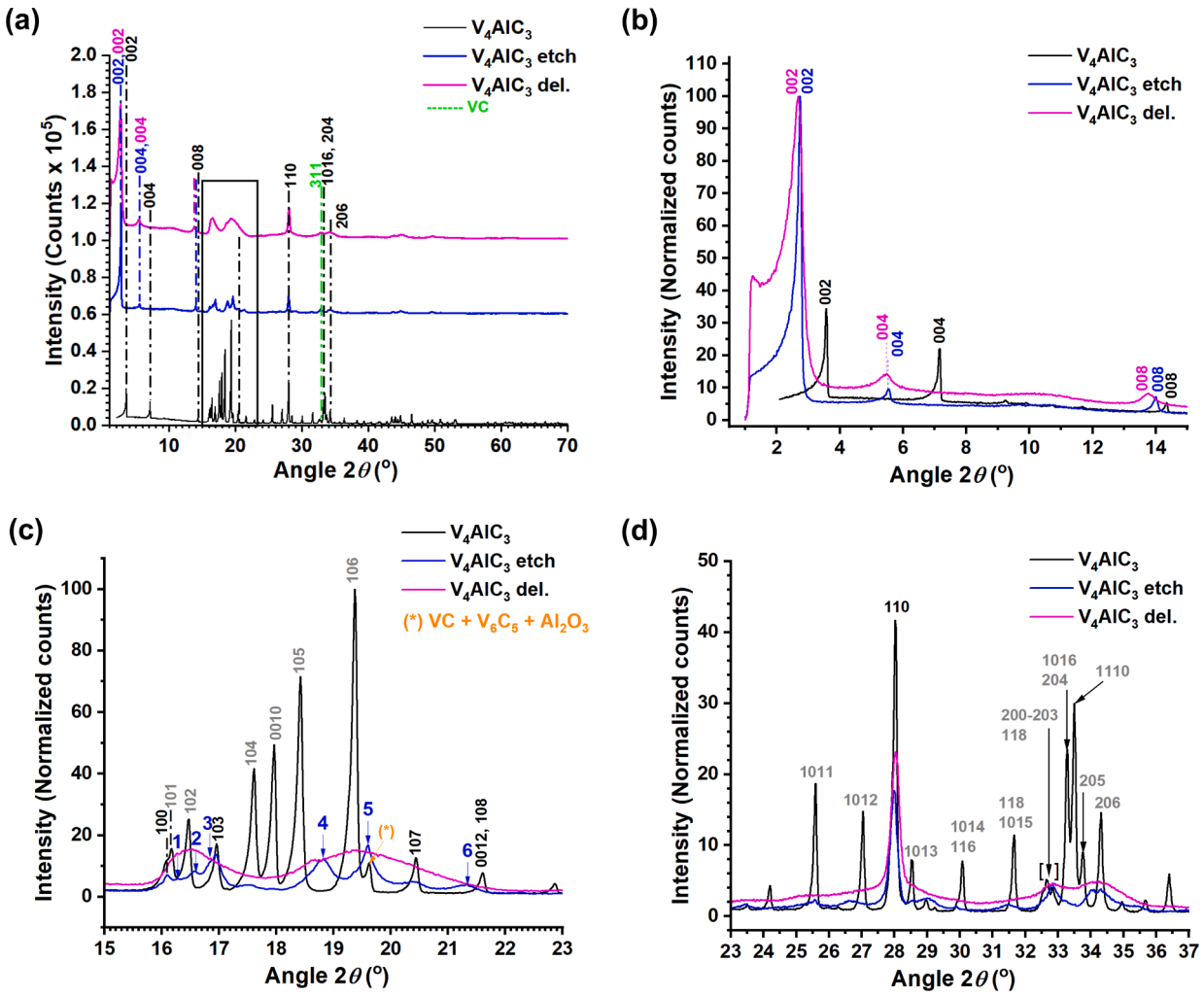

Fig. 4. XRD patterns of V_4AlC_3 and corresponding etched and delaminated samples. (a) Full 2θ range patterns,(b-d) patterns in reduced 2θ regions - for (c) the 2θ marked with a square in (a). The labels indicate hkl reflections corresponding to each sample (color set on the legend). In (b) hkl reflections present in V_4AlC_3 but not on etched/delaminated material are marked (gray color).

is reached, the reflection 100 can be merged with h0l reflections [56], which could be the case here for the 100 and 101 reflection (Fig. 4c). Decrease of intensity and broadening of h0l reflections has been observed as the 1 layer limit is reached [56]. A decrease of intensity of reflections can also be induced by interlayer translation [56]. Interlayer rotation can lead to merging of h0l reflections and to shifts to lower or higher 2θ angles depending on the direction of the rotational axis [56]. Some of these instances of interlayer crystal disorders might be possible during etching of MXenes. Theoretical studies will be necessary to establish the precise crystal transformations taking place upon etching of MXenes. What is important is that such merging and broadening of h0l reflections is a feature of an etched material that successfully leads to delamination.

Upon delamination, the merging of hkl reflections resulted in two broad intensities at $2\theta = 15.6–17.3\ ^\circ$ and $2\theta = 17.3–23.5\ ^\circ$ (Fig. 4c).

Amongst the h0l reflections, the 103 reflection is the most stable upon etching. This is also the case for etched V_2AlC reported in our previous work [53]. Thus, this reflection can be used as a marker of the degree of etching, which upon delamination is totally transformed into a broad intensity.

The 100 reflection is expected to be insensitive to the number of layers [56] and thus, should be present in delaminated material. This is the case for etched and delaminated V_2AlC [53]. In the case of etched V_4AlC_3, due to merging with the h0l reflections, the 100 reflection is affected by the reduction of number of layers upon etching and delamination.

At $2\theta = 25–40\ ^\circ$, the reflection 110 (V_4AlC_3) was pervasive upon etching and delamination (Fig. 4a). This is the case also for etched and delaminated materials derived from V_2AlC [53], reported in our previous work and delaminated $Ti_3C_2T_z$ [57]. Previous studies in other 2D nanomaterials, established that the 110 reflection is present in single-layer material, it is not sensitive to neither the number of layers of the material nor to crystal disorder [56]. Rather, broadening is induced by crystal lateral dimension reduction [56]. Here, this reflection did not change position but was slightly broadened upon etching and delamination. So, the insensitivity to the number of layers and to the crystal disorder is confirmed. Since the broadening of reflection was quite mild upon etching and delamination, we cannot correlate it with reduction of crystal lateral size.

3.3. Charge storage properties

The charge storage properties of $V_4C_3T_z$ film electrodes were studied in a half-cell set up and in 3 M H_2SO_4. The charge storage was investigated in negative electrochemical windows. It is known that MXenes oxidize in positive electrochemical windows in aqueous electrolytes [16]. Cyclic voltammograms (CVs) were run at 0.5 mV s^{-1} scan rates from open circuit potential (OCP), 0.38 V vs. Ag/AgCl), to − 0.4 V vs.

Ag/AgCl in 0.25 mV steps (Figure S3). Clear current peaks due to hydrogen evolution were encountered beyond − 0.35 V vs. Ag/AgCl, which was selected as the negative limit for stable charge storage (Figure S3). Then, the electrochemical performance was investigated in the − 0.35 to 0.4 V selected electrochemical window. CVs were performed at increasing scan rates, from 0.5 to 500 mV s^{-1} (Fig. 5a–c). A maximum capacity/capacitance were achieved at 1 mV s^{-1}. The values for cathodic capacity/capacitance at this scan rate were 202.4 C g^{-1}/0.52 C cm^{-2}/ 647.8 C cm^{-3} and 269.8 F g^{-1}/ 0.67 F cm^{-2}/863.7 F cm^{-3} (Fig. 5d–f). The corresponding anodic values were 193.8 C g^{-1}/0.49 C cm^{-2}/ 620.6 C cm^{-3} and 258.5 F g^{-1}/ 0.66 F cm^{-2}/827.4 F cm^{-3} (Fig. 5d–f). Notice that the capacitance reported by XAS measurements and measured by potentiostatic steps was even higher (469.6 F g^{-1}), as described in Section 3.4.

The Coulombic efficiency (CE) varied with scan rate (Fig. 5d–e). At scan rates below 10 mV s^{-1}, the anodic charge storage was lower than the cathodic charge storage, the CE was 91.5 % at 0.5 mV s^{-1} (Fig. 5e). At higher scan rates, the opposite was true (Fig. 5d). At the same time, more charge was stored at a CV scan rate of 1 mV s^{-1} than at 0.5 mV s^{-1} (Fig. 5e). The phenomena at low scan rates are interlinked and can be explained as follows. First, electrolyte access to active materials plays a role. It is known that 2D nanomaterials tend to restack once in film form. On pristine film electrodes, this condition prevents electrolyte access to active sites. The effect is enhanced at low CV scan rates where deep electrode sites, difficult to reach, contribute substantially to charge storage. In order to improve electrolyte access, an "activation" procedure is commonly performed, which consists on doing a number of CV cycles at medium range scan rates, e.g. 10 mV s^{-1}, prior to tests of interest. This promotes electrolyte infiltration and, thus, "stabilization" of charge storage, i.e. an increase until a constant charge is achieved. This, however, can alter the OCP and the electrochemical signature of the first cycles of following tests of interest. Here, activation was performed for 10 cycles at 10 mV s^{-1}. Second, ion transport phenomena at the very low scan rate play a role. In cyclic voltammetry, as the scan rate decreases, the diffusion layer thickness increases and the flux of electrolyte reactants towards the electrode decreases [58]. This brings low CV currents over large charge storage times. Charge storage over long time periods allows an increased utilization of deep active sites within the electrode where ion transport is diffusion controlled. Thus, as the scan rate decreases, the total stored charge should increase. However, since low scan rates imply a lower flux of electrolyte ions moving through an increasingly thicker diffusion layer [58], representing a diffusion resistance, there is a threshold scan rate where ion "starvation" takes place. In this scenario, charge storage is limited by the ions reaching active

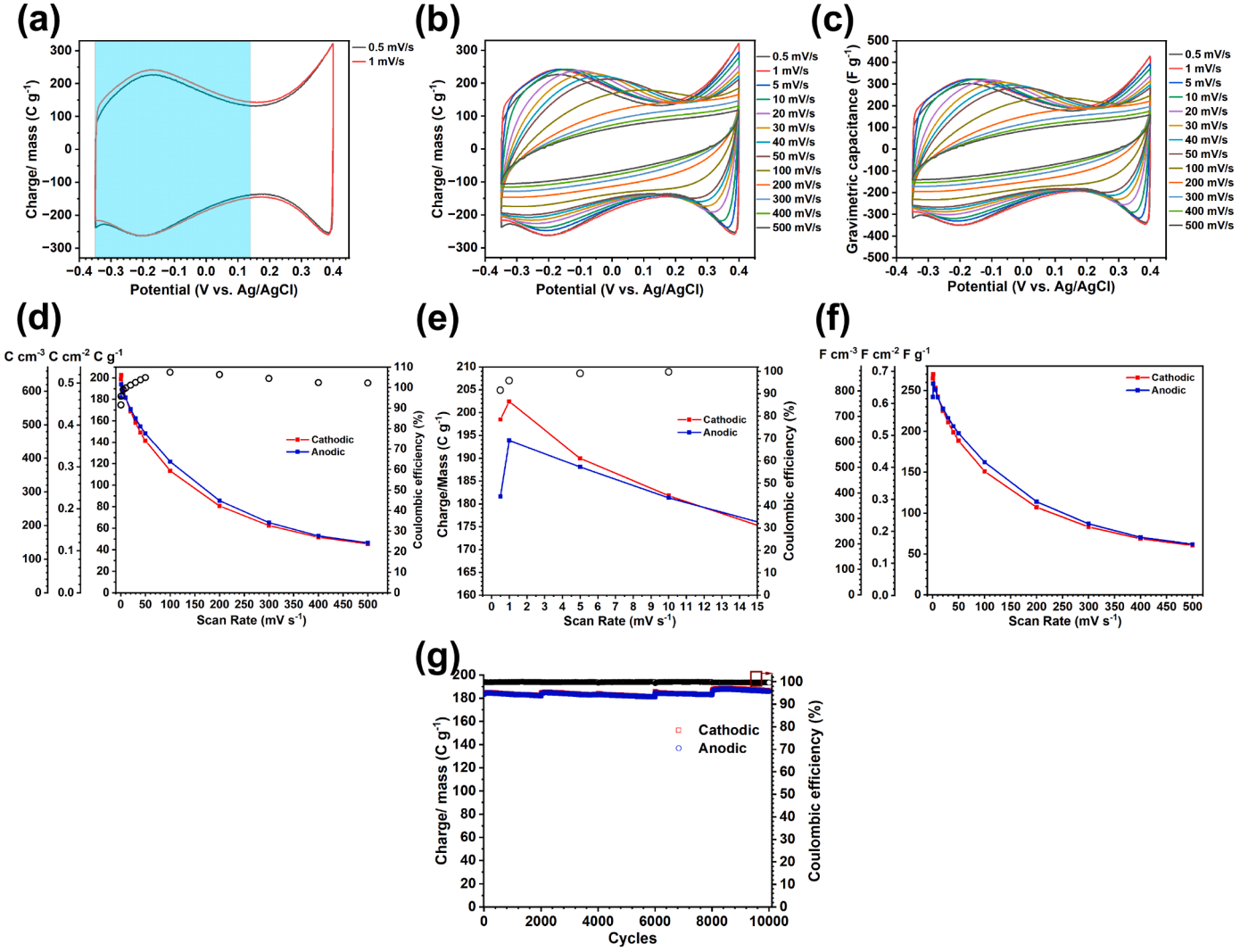

Fig. 5. Cyclic voltammetry tests of $V_4C_3T_z$ film electrodes in a half-cell set up using Ag/AgCl as reference electrode and 3 M H_2SO_4 electrolyte. CVs (second cycle) at (a) 0.5 and 1 mV s^{-1} and (b)-(c) 0.5 to 500 mV s^{-1}, (d-e) corresponding charge storage and (f) capacitance vs. scan rate curves - notice that (e) is the inset of (d) -, (g) charge storage vs. cycle number curves calculated from CVs run at 10 mV s^{-1}. The charge storage is presented in (a)-(b) C g^{-1} and (c) F g^{-1}. In (a) the potential region affected by ion starvation, and where charge storage processes involve mass transport control (as further explained in section 3.4) is colored.

sites of the electrode resulting in a lower overall charge storage. For the $V_4C_3T_z$ film electrode, this threshold scan rate seems to be 1 mV s^{-1}. This phenomena affected both cathodic and anodic processes, but the effect was larger for anodic processes (Fig. 5e). In addition, from the CVs it is clear that the difference in charge storage lies at a potential region below 0.14 V vs. Ag/AgCl (colored region in Fig. 5a). In the following sections, we confirm that in this potential region, indeed, charge storage consists of pseudocapacitance plus processes that involve mass transport control (Section 3.4). The fact that anodic processes were more affected than cathodic processes in terms of the overall charge storage achieved and the largest drop of charge storage at the lowest scan rate, indicated enhanced mass transport issues for ion-deintercalation.

At scan rates higher than 10 mV s^{-1}, surface-based processes must be responsible for the cathodic/anodic charge storage differences observed. However, the effect of residual currents, explained in Section 3.4, when measuring a CV must be kept in mind as an artifact introduced by the nature of the CV technique that is enhanced at high cycling rates [59].

On the other hand, a good rate performance was achieved up to 100 mV s^{-1}, where 62.8 % of the cathodic capacity was retained (Fig. 5d). Cycling performance, evaluated using CV at 10 mV s^{-1}, showed stability up to 10,000 cycles with a CE of 91.7–91.8 % and capacity fluctuation < 3.9 % (Fig. 5g).

The $V_4C_3T_z$ film electrodes were also studied using galvanostatic cycling with potential limitation (GCPL) at current rates of 0.25 to 30 A g^{-1} (Fig. 6). At 0.25 A g^{-1} current rate, the cathodic storage was much larger than anodic storage (CE of 95 %), and there was a downward trend of both stored discharge and charge (Fig. 6a). This is in agreement with the findings by CV tests at low scan rates and, as previously discussed, are attributed to diffusion-controlled processes. At the higher rate of 1 A g^{-1}, the CE was 98.2 %. Such small a small irreversibility might be linked to reduction of surface oxides present in the as-synthesized $V_4C_3T_z$ film or to irreversible reactions of surface chemical groups. Upon reversal of the current rate back to 0.25 A g^{-1}, the same capacity than obtained in the GCPL step 1 was recovered, although with the same CE.

Charge-discharge curves at 0.25 to 2 A g^{-1} showed no particular shape differences as the scan rate increased (Fig. 6b,c). The GCPL curves reflected the same electrochemical activity indicated by CVs, especially at 0.25 A g^{-1} (Fig. 6b). Charge-discharge curves at 5 to 30 A g^{-1} showed a very small ohmic drop from 0.37–0.40 V vs. Ag/AgCl, indicating good electrical properties of the electrode (Fig. 6c).

It is clear that the $V_4C_3T_z$ film electrode is capable of high rate performance up to 30 A g^{-1} (equivalent to ca. 200 mV s^{-1}), achieving 100 C g^{-1} (Fig. 6a). A GCPL cyclability test at 10 A g^{-1} showed 10,000 cycles without capacity fading and a CE of 99.6 % (Fig. 6d). The capacity changes every 2,000 cycles are due to re-starting of the cycling test where new electrolyte was supplied to the cell. The capacity first dropped and then increased, due to activation processes over cycling. A similar effect was observed in the cycling test by CVs where the charge storage increased upon addition of new electrolyte (Fig. 5g).

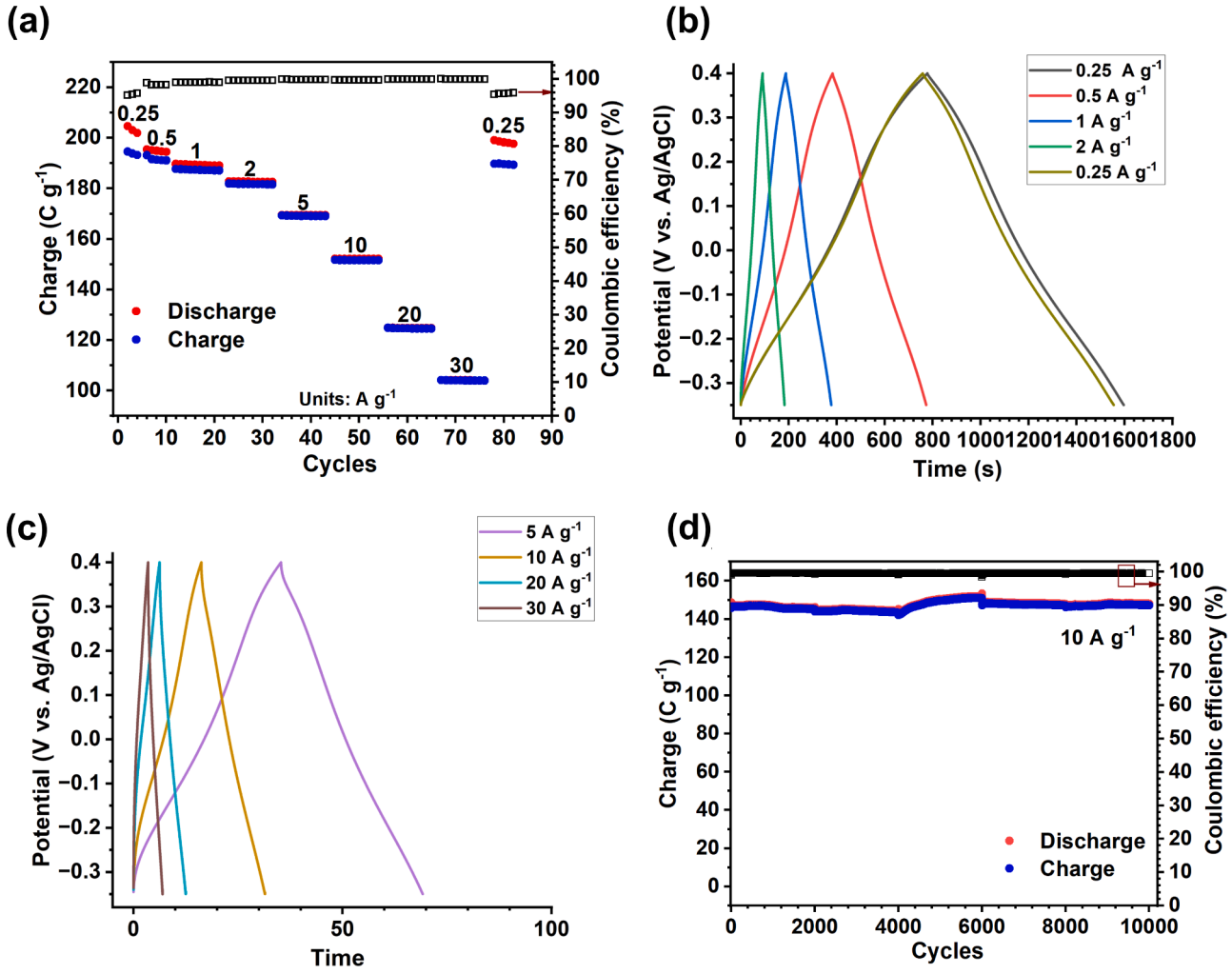

Fig. 6. GCPL tests of $V_4C_3T_z$ film electrodes performed in a half-cell set up using Ag/AgCl as reference electrode and 3 M H_2SO_4 electrolyte.(a) Charge storage vs. cycle number curves obtained from GCPL tests at various current rates, (b-c) corresponding GCPL curves(second cycle), (d) Charge storage vs. cycle number curves for a cycling stability test performed at 10 A g^{-1}.

Before putting in context the energy storage performance of the presented material versus other previously reported V_4AlC_3-derived electrodes, it must be highlighted that often direct comparison is not suitable due to very different synthesis and electrochemical testing conditions. The chemical and physical properties of a MXene have a strong dependence on synthesis procedures and on the properties of MAX precursors [53]. Therefore, one should be cautious when comparing the nominally "same" MXenes across literature. The capacitance will naturally vary with differences in electrochemical windows; capacity/capacitance per unit mass will vary with mass loading of electrodes and use/or not of binders and the nature of current collectors; volumetric capacitances will vary with electrode thickness - not always stated by authors; and, in general, electrode performance will vary with electrode composition and architecture derived from manufacture procedures.

Most previous work on application of V_4AlC_3-derived materials in energy storage report on multilayer, rather than delaminated material [33–35] (Table S1). Multilayer material, consists of partially etched materials, that may be a combination of unetched MAX platelets and partially etched material of $V_{4-x}Al_{1-y}C_3T_z$ composition [53]. In general, multilayer material has very different chemical and physical properties than fully delaminated material, including a poorer electrical conductivity. This is reflected on previous works where a conductive agent is added to electrodes to achieve meaningful storage [33–35] (Table S1) and on poor rate performance [33]. Another disadvantage of multilayer material is the need to add binders to manufacture electrodes and to achieve electrode integrity. Conductive additives and binders undermine the capacitance per unit mass and volume of electrodes. In other cases, multilayer material is deposited onto current collectors [33]. In this sense, the free-standing electrically conductive film electrodes presented here have clear advantages. No binders or conductive additives are used. A higher capacitance per unit mass than in most previous works [33–35] was achieved (Table S1). Free standing film electrodes based on 2D nanomaterials offer scope for application in micro-/-wearable electronics where capacitance per unit volume is important -not reported for multilayer material based electrodes [33–35]. The rate performance was outstanding, compared to a poor performance of multilayer material based electrodes that show a very poor electrical conductivity [33]. The same can be said about cycling stability (Table S1), here demonstrated up to 10,000 cycles.

Comparison of $V_4C_3T_z$ vs. other delaminated MXenes is relevant (Tables S1, S2). A main work reports on V_2CT_z tested in 1 M H_2SO_4 in a 0.8 V electrochemical window [24]. The electrochemical window is of the same magnitude than here used and the mass loading was reported as 1.9 mg cm^{-2}, lower than 2.56 mg cm^{-2}used here. The electrode thickness was not reported. The capacitance reported was 487 F g^{-1} at 2 mV s^{-1}, almost twice the 269.8 F g^{-1} at 1 mV s^{-1}, here reported for $V_4C_3T_z$. This is explained by the difference in molar mass of V_2CT_z vs. $V_4C_3T_z$. This is a clear advantage of lower stoichiometry MXenes. However, the well known high sensitivity of V_2CT_z to oxidation is a clear disadvantage of this material. A solution for this issue has been proposed and consists on the use of salts to protect MXenes against oxidation [60]. Whereas this procedure might be an effective solution against MXene oxidation, it adds extra-processing steps and costs for real applications. In this sense, $V_4C_3T_z$ offers clear advantages. We have found $V_4C_3T_z$ to be much more stable than V_2CT_z, both in suspension and in film form. $V_4C_3T_z$ films were stable after 1 year kept in a glove box in inert environment.

As per volumetric capacitance, the $V_4C_3T_z$ electrodes here presented showed 863.7 F cm^{-3} at 1 mV s^{-1} for an electrode of 8 μm. $Ti_3C_2T_z$ clay electrodes had 900 F cm^{-3} (and 245 F g^{-1}) at 2 mV s^{-1} in 1 M H_2SO_4, for 5 μm electrodes [31]. Numbers are not directly comparable, but are in the same range. Tuning of nanosheet morphology to improve ion transport, introducing pores, had led to higher charge storage of $Ti_3C_2T_z$ [14]. The same could be applied to improve even further the charge storage of $V_4C_3T_z$ electrodes. Another $M_4C_3T_z$ MXene, $Nb_4C_3T_z$ had 1075 F cm^{-3} at 5 mV s^{-1} in 1 M H_2SO_4 in a 1 V electrochemical window [61]. The thickness of these electrodes was not reported. The slightly larger storage can be explained by the slightly larger electrochemical window. However, as per the CVs of this material, an issue of resistivity is in place [61]. The electrical conductivity of V-based MXenes is known to be higher than Nb-based MXenes [18,36]. For instance, Nb_2CT_z and $Nb_4C_3T_z$ have an electrical conductivity of 25 S cm^{-1} and 90 S cm^{-1}, respectively [18], whereas V_2CT_z and $V_4C_3T_z$ have an electrical conductivity of 1201 S cm^{-1} and 1272 S cm^{-1}, respectively [36]. As compared to mixed MXenes, $Mo_{2.7}V_{1.3}C_3T_z$ showed a volumetric capacitance of 860 F cm^{-3} in a 1 M H_2SO_4 electrolyte and in a 0.85 V electrochemical window [27] (Tables S2), similar to here found for $V_4C_3T_z$. However, acidified sulfate-based electrolytes were preferred over the acidic 1 M H_2SO_4, where the volumetric capacitance was lower (400 F cm^{-3}) despite larger electrochemical windows [27]. This was most probably due to the better cycling stability of this Mo-based MXene in neutral/acidified electrolytes than in 1 M H_2SO_4. The high cycling stability of $V_4C_3T_z$ in the highly acidic 3 M H_2SO_4 electrolyte, where, generally, MXenes store much more than in neutral electrolytes, is an advantage of this V-based MXene versus Mo-based MXenes.

A full cell using the $V_4C_3T_z$ as negative electrode and an activated carbon as positive electrode was tested in a 1.35 V working window. Details of balance of mass of positive and negative electrodes are given in the Supporting Information (Section S7). CVs, charge and capacitance per unit mass, area and volume vs. scan rate curves, and Ragone plots per unit mass and volume are shown in Figure S5. Maximum energy and power per unit mass of 14.7 Wh kg^{-1} (at 0.019 kW kg^{-1}) and 9.74 kW kg^{-1} (at 7.3 Wh kg^{-1}) were achieved. Volumetric energy and power are the metric of interest for miniaturized devices. Maximum energy and power per unit volume of 10.5 mWh cm^{-3} (at 0.014 W cm^{-3}) and 7.0 W cm^{-3} (at 5.2 mWh cm^{-3}) were achieved. In the context of other MXene-based full cells, a previously reported $Ti_3C_2//\alpha$-MnO_2 cell achieved 16.80 mWh cm^{-3} at 0.13 W cm^{-3} in a 21 molal potassium acetate electrolyte in a 2.2 working window [62]. The full cell here presented is a proof of concept. Due to the lower density of a carbon electrode, as compared to the 2D MXene-based electrode, it is not the suitable positive electrode for a device of optimized performance per unit volume. Future work should involve finding a suitable positive electrode.

3.4. Charge storage mechanisms

The nature of the charge storage mechanisms undergone by $V_4C_3T_z$ film electrodes, tested in a half-cell set up, were studied using electrochemical methods and *in situ* XAS.

3.4.1. Electrochemical kinetics and mass transport

First, predominant charge storage processes were investigated via CV and theoretical models. Up to date, two well known models consider energy storage contributions from capacitive processes (EDLC or pseudocapacitive) controlled by electrochemical kinetics and faradaic processes controlled by mass transport, diffusion in this case. In a EDLC or a pseudocapacitive process, the response current I is proportional to the rate of change of applied potential or scan rate ν. In a process controlled by diffusion, I is proportional to $\nu^{0.5}$, if semi-infinite boundary conditions apply[2]. In our case of study, semi-infinite boundary conditions hold as per the use of planar macroelectrodes [58]. Model 1 considers $I = k\nu^b$ (Equation 9), where k and b are unknown constants. According to the previous description, b = 1 describes capacitive/pseudocapacitive

[2] The relationship of measured current with the flux of stored species (ions) describes charge storage, where the flux can be dominated by electrochemical kinetics or mass transport. In the latter case, the flux is defined by Fick's first law [58]. Solving the second Fick's law using semi-infinite boundary conditions leads to the Cottrell equation where the current is inversely proportional to time, or equivalently, directly proportional to the square root of scan rate [58].

processes and b = 0.5 describes diffusion-controlled processes. Model 2, considers a parallel combination of capacitive and diffusion-controlled current terms, $I = k_1\nu + k_2\nu^{0.5}$ (Equation 10), where k_1 and k_2 are unknown constants [63]. The connection in parallel of these terms, implies that charge storage takes place in a capacitive manner at the surface of the electrode and in a diffusion-controlled manner at interior sites of the electrode [63]. Here, we make use of these models while explicitly establishing their limitations. This is important because their use in a generalized manner without establishing limits of applicability can lead to the wrong interpretation of experimental data.

Model 1 was applied to CVs from 0.5 mV s^{-1} to 100 mV s^{-1} (Figure S6). The first observation is that this model applies up to a limiting scan rate where log(I) vs. log (ν) curves deviates from linear behavior at potentials near to the limits of the potential window of interest (Figure S6b,c). In consequence, b values, i.e. the derivative of log(I) vs. log (ν) curves, deviate from b = 1 to take lower values as the scan rate increases (Figure S6d,e). Such deviations are explained by the cell potential $V = IR_u$, where R_u is the uncompensated cell resistance [64]. This potential becomes more important as scan rate increases [64] and causes the current distortions observed at potentials near to the potential window limits of interest (Figure S6a). In consequence, the application of models 1 and 2 are restricted up to potential limits where such CV distortions become insignificant. The larger the scan rate the lower the potential window where the models apply (Figure S6). Here a scan rate of 10 mV s^{-1} was selected as a suitable limit where models 1 and 2 apply (Fig. 7a). For model 1, the potential limits of application were selected as (0.34 V to − 0.3 V) for the cathodic currents and (0.4 V to − 0.28 V) for the anodic currents. For model 2, the selected potential limits were selected as (V_{lim1} = 0.36 V to V_{lim2} = − 0.28 V) (Fig. 7a).

For model 1, log(I) vs. log (ν) curves followed linear trends (Fig. 7b,c) and upon linear fitting the b values were calculated (Fig. 7f). The accuracy of the fitting was verified with $R^2 = 0.9988$ to 1.0000. This model estimated $0.9632 < b < 1.0092$ for the cathodic currents and $0.9554 < b < 1.0407$ for the anodic currents. The latter with an slight overestimation $b > 1$, at a 0.18 V to − 0.2 V vs. Ag/AgCl potential range.

For model 2, $I/\nu^{0.5}$ vs. $\nu^{0.5}$ curves showed linear trends (Fig. 7d,e).

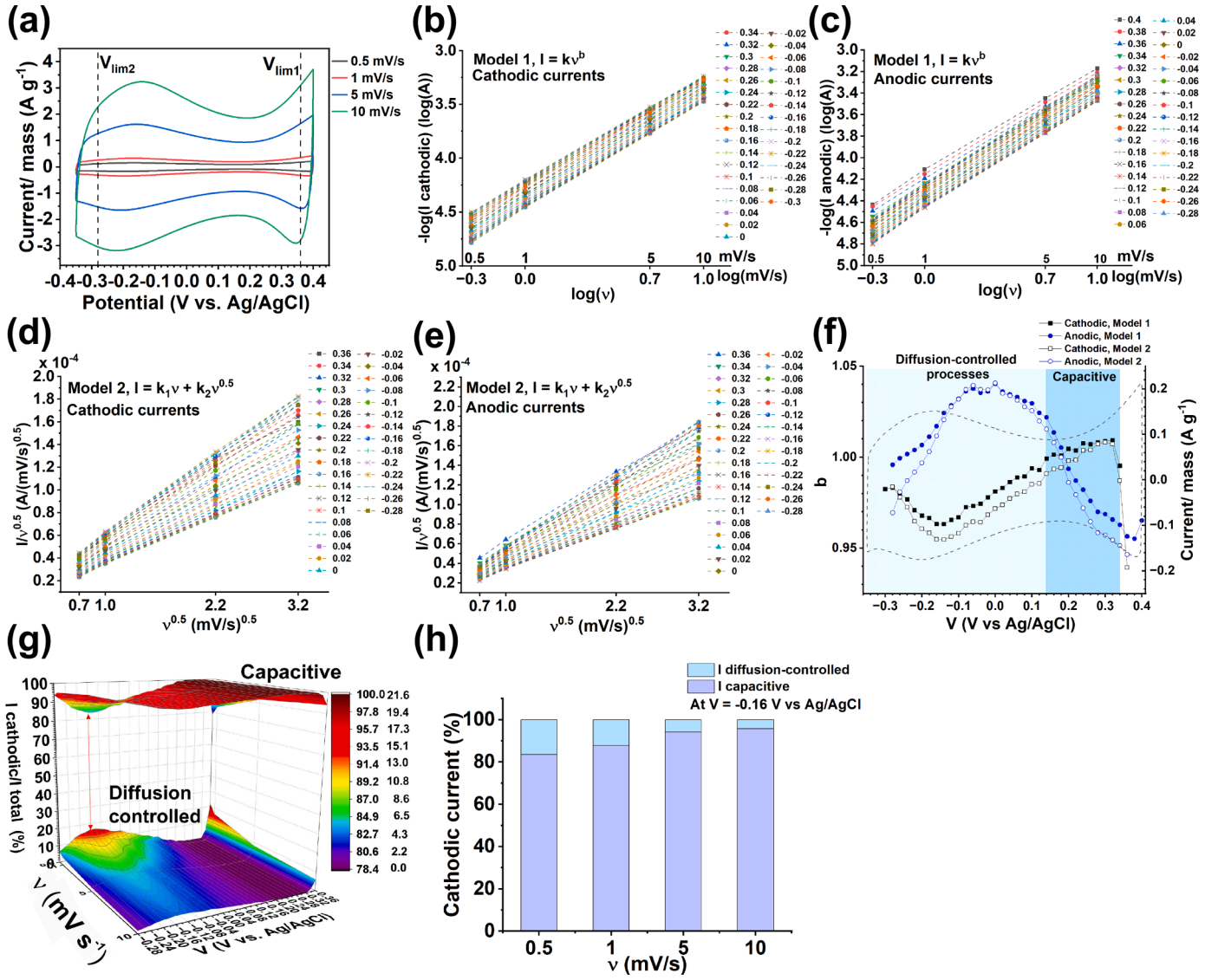

Fig. 7. Use of models 1 and 2 for the analysis of CV experimental data. (a) CV at 0.5 mV s^{-1} to 10 mV s^{-1} showing the potential window limits used for analysis of model 2 (V_{lim1} = 0.36 V and V_{lim2} = − 0.28 V), (b) cathodic and (c) anodic log(I) vs. log (ν) experimental curves (model 1), (d) cathodic and (e) anodic $I/\nu^{0.5}$ vs. $\nu^{0.5}$ experimental curves (model 2), (f) calculated b value from models 1 and 2 and CV at 0.5 mV s^{-1} -potential regions where b = 1 and and b < 1 according to determinations from cathodic currents are marked in colors, (g) 3D surface plots of the percentage of capacitive and diffusion-controlled cathodic current calculated from model 2, at all considered scan rates and over the full considered potential range (V_{lim1} and V_{lim2}), the red arrow indicates V = − 0.16 V (h) graph of the percentage contributions of capacitive and diffusion-controlled cathodic currents calculated from model 2 at V = − 0.16 V.

The accuracy of the fitting was verified with $R^2 = 0.9880$ to 1.000. A b value for this model was defined as the slope of log(I_{calc}) vs. log (ν) curves, where I_{calc} is the current calculated by model 2 (Equation 10). The b values follow the same trend than in model 1 (Fig. 7f). As in model 1, in the case of anodic currents, the b values were slightly overestimated in the same 0.18 V to − 0.2 V vs. Ag/AgCl potential range. A comparison of experimental anodic and cathodic currents in this potential range confirmed that, indeed, anodic currents are slightly larger than cathodic currents at $\nu \geq 5$ mV s^{-1} - not to confuse with the overall achieved cathodic and anodic charge, in which case the cathodic charge was larger than the anodic charge. This led to the slightly overestimated b values calculated by the two models, and confirmed its experimental, rather than fitting error, origin. This phenomenon could be attributed to residual currents coming from measurements [59], slightly more significant for anodic currents. When running a CV, a potentiostat applies a potential step V_i over a given time step (set by the scan rate). When advancing to the next potential step V_{i+1}, the total measured current $I = I_i + xI_{i-1}$, where $0 < x < 1$. Thus, the current response of a CV may be overestimated and this effect will be larger as the scan rate increases. The latter was indeed confirmed, the overestimation of b values increased, and experimental anodic currents were higher than cathodic currents, as larger scan rates were included in the analysis of the models. Therefore, for the application of these models, selecting a sufficiently low scan rate is of critical importance, as well as, to be aware of artifacts coming from measurements.

Nevertheless, Model 1 and 2 describe the system as storing charge under two regimes (Fig. 7f). Given the above observations, interpretation of results is more reliable in terms of the cathodic currents. The b values of cathodic currents describe capacitive processes (that could be EDLC or pseudocapacitance) at 0.32 V to 0.14 V vs. Ag/AgCl with b values of 0.9991–1.0092. At lower potentials the b values decreased to a minimum b = 0.9548 at V = − 0.16 V vs. Ag/AgCl, around the maximum of the cathodic current (Fig. 7f) and where, according to model 2, a maximum (but still low) contribution of diffusion-controlled processes took place (Fig. 7g). Further EIS and XAS studies (below) allowed to determine further details of predominant specific charge storage processes at these potential regions.

An important observation of model 2 is that it, fundamentally, imposes a transition from a high to a low contribution of diffusion-controlled processes at low and high scan rates, respectively [65]. The opposite is true for capacitive processes [65]. These trends were verified for our system of study (Fig. 7g-h), which, accordingly, should not be interpreted beyond the mathematical nature of the model itself. It simply states that the system of study could be interpreted with model 2 (describing charge storage at two different sites, surface and bulk, of the electrode) but not necessarily in a unique manner. Model 2 must be understood as a basic choice for interpretation of charge storage mechanisms. More sophisticated models and further mathematical treatment considering the complexity of real electrodes [65](e.g. the presence of nanochannels in 2D materials based electrodes, electrolyte access at different sites and intrinsic physical and chemical properties) are yet to be developed.

3.4.2. Studies by staircase potentio-electrochemical impedance spectroscopy

Next, charge storage mechanisms were further studied using staircase potentio-electrochemical impedance spectroscopy (SPEIS). This technique allows EIS measurements during a CV scan and at successive potential steps allowing to study the electrochemical kinetics/mass transport properties [49–51]. Here, EIS was measured every 25 mV along the CV of interest (− 0.35 V to 0.4 V vs. Ag/AgCl) (see Experimental methods for further details). Impedance parameters are reported in 3D plots as a function of frequency and electrode polarization potential and considering separately data from the cathodic and anodic CV scan. Unlike the previous method based on models 1 and 2, the SPEIS method allows an analysis over the entire electrochemical window of interest.

3D Nyquist plots (Figures S7a-d) report on processes dominated by semi-infinite linear diffusion at high frequencies (e.g. > 0.33 Hz) and by capacitive processes at low frequencies (e.g. < 0.33 Hz) at all potentials. 3D $|Z|$ vs. frequency vs. potential (Figure S7e-f) and -Phase angle (ϕ) vs. frequency vs. potential (Fig. 8a-b) plots showed a resistor behavior (Z' invariant with frequency and $-\phi = 0$ ° at e.g. 4.75 kHz < frequencies < 250 kHz) to a transition region (frequencies < 4.75 kHz), where the - ϕ and $|Z|$ increased with decreasing frequency, to reach $-\phi$ close to 90 °, typical of a pure capacitor, and maximum $|Z|$ at the lowest frequency of 4 mHz. This behavior was consistent across all potentials, both in the cathodic and anodic CV regions.

The capacitance of the system of study was calculated considering that the total complex impedance Z = Z' + jZ" is due to a capacitor with dissipative losses (Eq. (5)) [52]. Accordingly, the real C' and and imaginary C" components of a complex capacitance can be calculated from Eqs. (6) and (7). This is a simplified model of a supercapacitor where C' is the capacitor response and C" represent the resistive components that lead to energy losses [52], such as porosity (ionic resistance) and contact resistance [66]. The suitability of this model is limited to account for overall C' and C"contributions [52].

3D C' vs. frequency vs. potential plots showed and onset of capacitive contribution at a frequency < 4.3 Hz that reached a maximum at the lowest frequency of 4 mHz, in both, the cathodic and anodic regions of the CV (Figs. 8a-c). At the lowest frequency, C' had two maxima at 0.4 V and − 0.225 V vs. Ag/AgCl and a minimum at 0.15–0.175 V vs. Ag/AgCl (Fig. 8c). The -Phase angle vs. potential curves at a frequency of 4 mHz shows the inverse trend showing minima values close to 90 ° at 0.4 V and − 0.225 V vs. Ag/AgCl and a maximum at 0.025–0.15 V vs. Ag/AgCl (Fig. 8f). On the other hand, the inverse frequency at $-\phi = 45$ °, at which the Z' = Z", an so C' = C" (Eqs. (6) and (7)), is a convenient time $t_{\phi=45°}$, to evaluate the onset of the capacitive response. This time $t_{\phi=45°}$ reached maxima at 0.4 V and at − 0.225 V vs Ag/AgCl potentials and a minimum at 0.15–0.175 V vs. Ag/AgCl (Fig. 8g). Analysis of these variables together with changes in oxidation states determined by XAS (see next section) allowed to establish predominant charge storage processes at specific potential regions, which are indicated in Fig. 8c,f,g.

Another aspect of the $t_{\phi=45°}$ vs. potential curves is worth discussing. The trends of cathodic and anodic regions were consistent but values slightly varied across potential regions where either anodic or cathodic values were higher (Fig. 8g). The switching potential points were the OCP (0.375 V), the minimum ("throat") of the CV (0.175 V) and maximum of the pseudocapacitive activity (− 0.225 V). The difference between anodic and cathodic $t_{\phi=45°}$ values described a slight electrochemical irreversibility. The switching at the cited potentials is most likely linked to transitions between charge storage mechanisms.

3D C" vs. frequency vs. potential plots (Figure S8a-b) describe the energy losses of the system and its maxima describe a characteristic frequency/time where half of the capacitive response C'/2 is achieved [52]. The time τ where C" reaches a maximum is known as dielectric relation time and is another suitable parameter to evaluate the capacitive response. The τ vs. potential curves followed a similar trend than $t_{\phi=45°}$ vs. potential curves (Figure S8a-b), thus, supporting conclusions about charge storage mechanisms.

3.4.3. In situ X-ray absorption spectroscopy studies

In situ XAS studies revealed further insights into charge storage mechanisms. The V-K XAS edge of V_4AlC_3 (Figure S9a) and pristine $V_4C_3T_z$ film (Fig. 9a) were measured along with V, V_2O_3, VO_2, V_2O_5 reference compounds. For the determination of oxidation states, a calibration curve was built using the reference compounds (Supporting Information, Section S10). The determined V oxidation state for V_4AlC_3 was + 2.08 and for the $V_4C_3T_z$ film was +3.59 (Figure S9b). For the investigation of charge storage mechanisms, the V-K XAS edge of $V_4C_3T_z$ electrode films was measured (Fig. 9a,b) while polarizing at potentials of

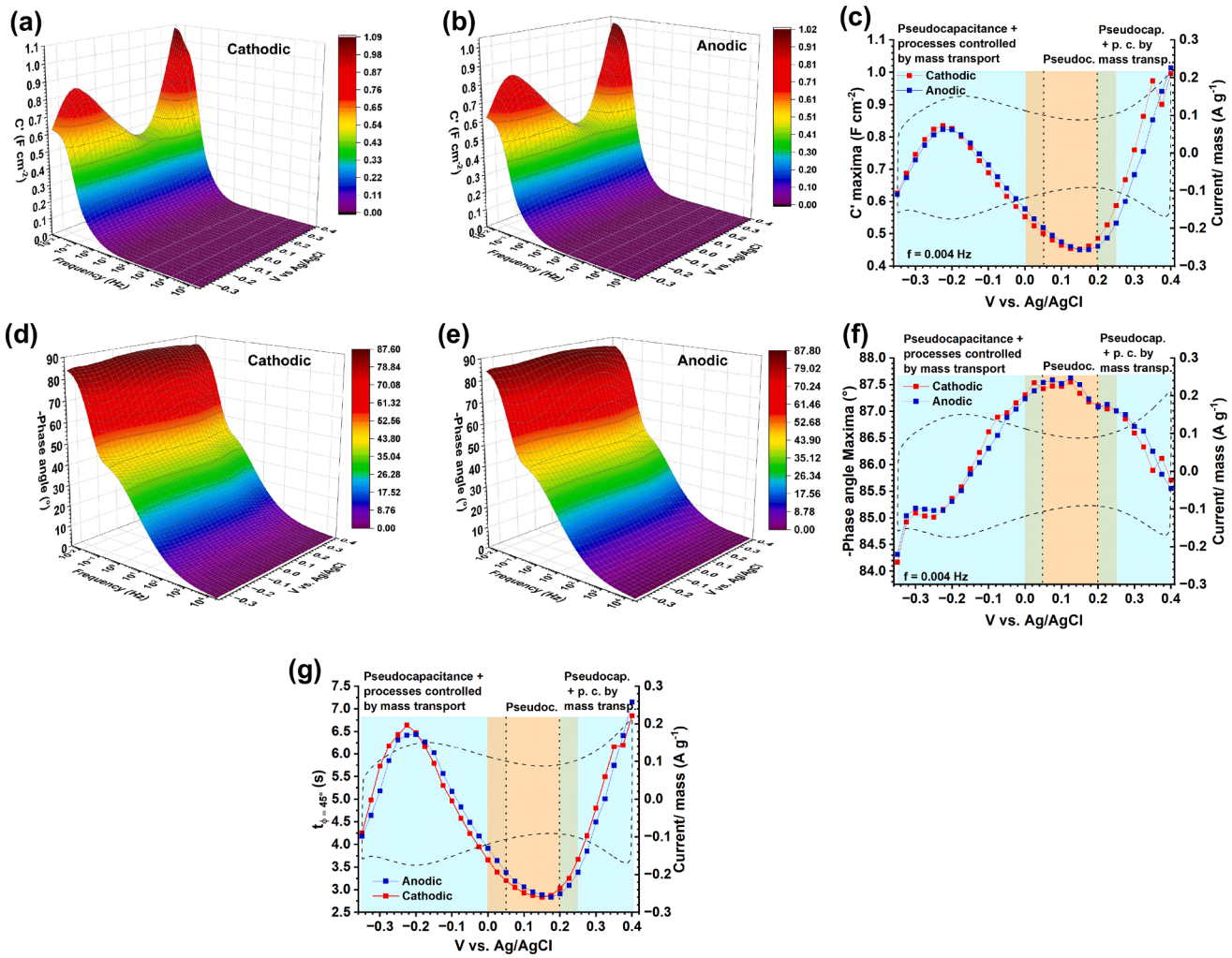

Fig. 8. Data derived from SPEIS studies performed during cathodic and anodic CV scans in a 0.4 to − 0.35 V vs. Ag/AgCl electrochemical window and using 25 mV steps. (a),(b) 3D C' vs. frequency vs. potential plots derived from EIS data during (a) cathodic and (b) anodic CV scans,(c) C' vs. potential curves during cathodic and anodic CV scans and at a frequency = 0.004 Hz, (d),(e) 3D-Phase angle vs. frequency vs. potential plots derived from EIS data during (d) cathodic and (e) anodic CV scans, (f) -Phase angle vs. potential curves, during cathodic and anodic CV scans and at a frequency = 0.004 Hz, (g) capacitive response ($t_{\phi=45^\circ}$) vs. potential curves during cathodic and anodic CV scans. A CV performed at 0.5 mV s^{-1} has been plotted for reference in (c),(f) and (g). Potential regions where particular charge storage mechanisms predominate (pseudocapacitance or pseudocapacitance plus processes controlled by mass transport) are indicated in color. EDLC has a contribution over the entire electrochemical window.

interest from OCP to − 0.35 V vs. Ag/AgCl (in reduction) and to 0.4 V vs. Ag/AgCl (in oxidation) for two CV cycles (Fig. 9d). Three spectra were measured during a 15 min potentiostatic step (Figure S10), but only the last two were used for calculations. The oxidation states were determined using the calibration curve.

The oxidation state of the V atoms at OCP was +3.57 (Fig. 9c,d). Upon polarization at 0.2 V vs. Ag/AgCl the oxidation potential did not change (Fig. 9c). Upon further reduction, the oxidation potential decreased down to +3.39 at − 0.35 V vs. Ag/AgCl (Fig. 9c,d). Upon oxidation, the oxidation state increased from +3.37 at − 0.32 V vs. Ag/AgCl to +3.63 at 0.4 V vs. Ag/AgCl (Fig. 9c,d). The oxidation states were reproducible during the second cycle of polarization (Fig. 9d). A last measurement at OCP reported a +3.60 oxidation state. Three more XAS spectra sets (3 x 3) were measured without polarization, the oxidation state remained stable at +3.60 (Fig. 9c). This indicated absence of self-discharge of the electrode at least for 45 min.

The change in oxidation states occurred over the entire operational electrochemical window. However, there are potential ranges where the changes in oxidation were larger than in others (Fig. 9d). A joint analysis of changes in oxidation states (Fig. 9d), real capacitance C' (Fig. 8c) and impedance phase angle (Fig. 8f) allowed to determine potential regions where specific charge storage mechanisms predominate (Fig. 10). The lowest changes in oxidation states (0.015 to 0.036) occurred at a 0.05 V to 0.25 V vs. Ag/AgCl potential range (Fig. 10). At this potential range, C' minima and -phase angle maxima took place (Fig. 10), indicating the lowest capacitive charge storage and near to ideal capacitive behavior, respectively. Here, according to models 1 and 2, b = 0.98–1 (Fig. 7f). Altogether, this indicated predominant pseudocapacitive processes in this potential region. A minor contribution of EDLC processes over the full electrochemical window is likely as per the 2D nature of the active material. At all other potential regions,(− 0.35 V to 0.05 V vs. Ag/AgCl) and (0.25 V to 0.4 V vs. Ag/AgCl), the changes in oxidation states were much larger (0.06 to 0.07) and C' maxima and -phase angle minima took place (Fig. 10). For the (− 0.35 V to 0.05 V vs. Ag/AgCl) potential region, a b = 0.95–0.98 (Fig. 7f). Therefore, at this potential region, we conclude that we have predominant pseudocapacitive processes plus a minor contribution of a process that is rate-limited by mass transport. For the (0.25 V to 0.3 V vs. Ag/AgCl) potential region, although b = 1 (Fig. 7f), the impedance data showed a -phase angle < 85.5–87.1 °, which discards the occurrence of only capacitive processes. Therefore, at this potential region, we conclude that we have the same predominant charge storage processes as in the (− 0.35 V to 0.05 V vs. Ag/AgCl)

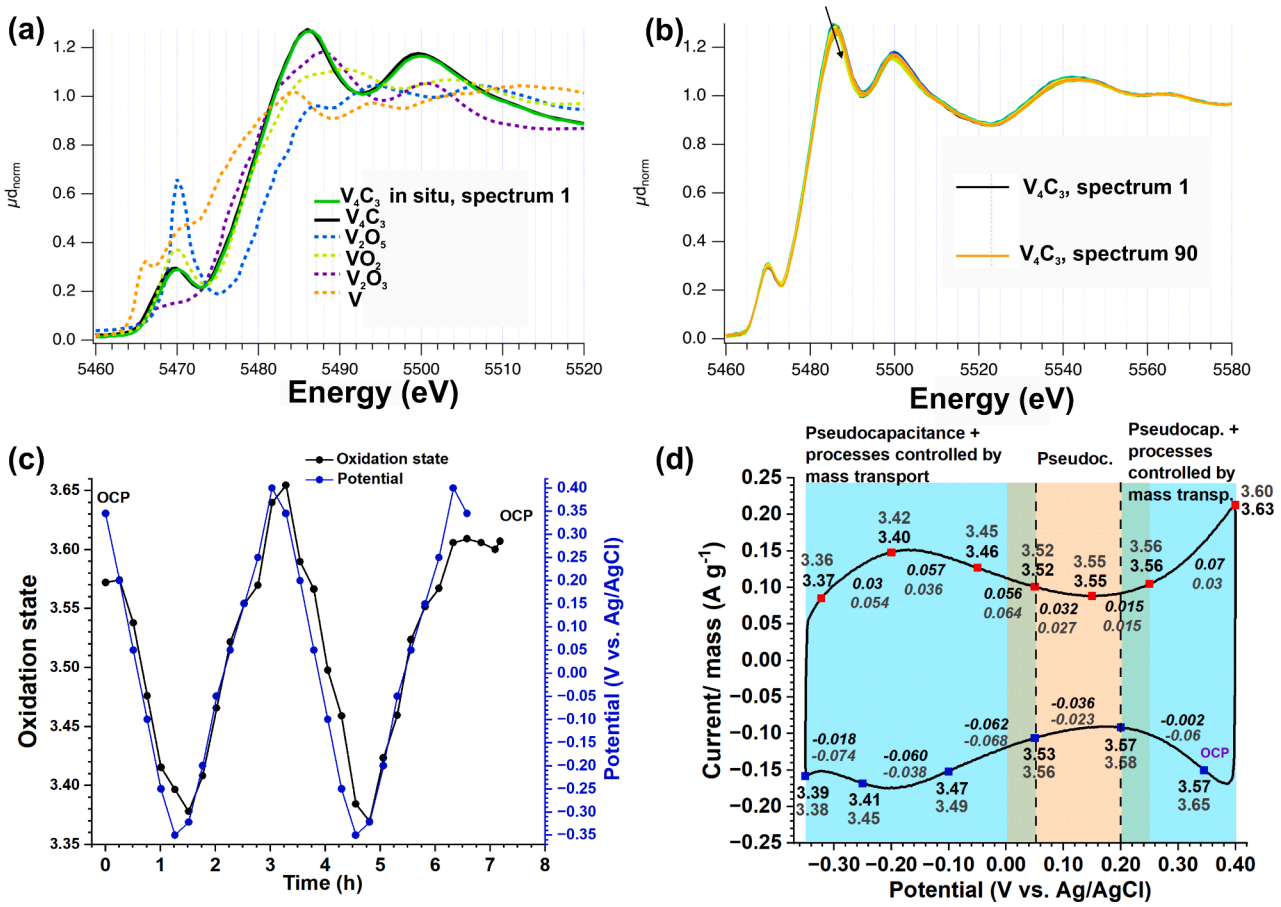

Fig. 9. (a) XAS spectra of a $V_4C_3T_z$ film, a $V_4C_3T_z$ film electrode measured *in-situ* and several reference compounds, (b) XAS spectra of the $V_4C_3T_z$ film electrode measured *in-situ*, (c) oxidation states and polarization potential vs. time curves, (d) a CV of the $V_4C_3T_z$ film electrode, measured *ex situ* at 0.5 mV s^{-1} scan rate, where potentials of polarization in reduction (blue) and oxidation (red) are indicated. The oxidation states determined by XAS are shown at the exterior of the CV next to the corresponding polarization potential. The changes in oxidation state are shown at the interior of the CV and in between the potentials of polarization. Black font indicates cycle 1 and gray font indicates cycle 2. Potential regions where particular charge storage mechanisms predominate (pseudocapacitance or pseudocapacitance plus processes controlled by mass transport) are indicated in color. EDLC has a contribution over the entire electrochemical window.

potential region. As described in the introduction of this work, ion intercalation phenomena in the confined interlayer spaces (nanochannels) of MXenes play an important role on charge storage processes [12–15]. Ion intercalation related phenomena include ion solvated/desolvated states, number of water/solvent molecules coordinating with the ions while intercalating in the confined spaces, number of water/solvent molecules pre-intercalated at the nanochannels and number of -OH functional groups present in the nanochannels [44,45]. Such events or combination of events can become rate-determinant in a charge storage processes. Whenever this happens, we observe overall charge storage processes that depart from capacitive (surface-based) processes. This is the case for deep sites of the electrode [13] and, as observed in our data, predominant at (− 0.35 V to 0.05 V vs. Ag/AgCl) and (0.25 V to 0.3 V vs. Ag/AgCl) potential regions. In this work, we refer to this fraction of the contribution to overall charge storage as processes controlled by mass transport (Fig. 10). Future work should elucidate the precise nature/dynamics of these mass transport-controlled events and the reason for occurrence at these precise potential regions.

Transitional potential regions were considered to be from 0.05 V to 0 V, according to -phase angle maxima, and from 0.2 to 0.25 V, according to changes in oxidation states and C' (Fig. 10).

The charge δQ per unit mass stored over the considered electrochemical window was calculated according to,

$$\Delta Q = \delta_i e^- \times \frac{Natoms}{mol} \times \frac{1}{M} \times 4 = 4\frac{\delta_i F}{M} \quad (11)$$

where δ_i is the numbers of electrons exchanged in the reduction/oxidation process per V atom, obtained from the XAS measurements (Table 2); e^- is the electron charge; N is the Avogadro number; F is the Faraday constant; and M and 4 are the molecular weight and number of V atoms in the $V_4C_3T_z$ compound, respectively. The capacitance was then calculated as $\Delta Q/\Delta V$ where ΔV is the electrochemical window.

For as-synthesized material, a molecular weight of 279.82 g mol^{-1} was calculated according to the composition of $V_4C_3O_{0.54}(OH)_{0.12}F_{0.8}Cl_{0.4}$. Since we do not know the precise stoichiometry of -O, -OH, -F and -Cl on $V_4C_3T_z$, and, to the best of our knowledge, it has not been previously reported, the quantities of functional groups were approximated according to previous studies that determined $Ti_3C_2O_{0.54}(OH)_{0.12}F_{0.8}$ from NMR studies [67]. In this study, $Ti_3C_2T_z$ was synthesized in 50 % HF, similar to the procedure here used. In another V-based MXene, V_2CT_z synthesized in 48 %HF, NMR studies confirmed a $V_2C(OH)_{1.2}F_1$ stoichiometry [68]. The former was used because we expect -O groups and a high degree of -F functionalization.The stoichiometry of -Cl, here Cl was confirmed by EDX studies, was considered half that for -F. Establishing the precise stoichiometry is not a trivial matter as it depends on synthesis conditions and post-processing steps, which will differ from study to study. Thus, these numbers must be taken as reference for the calculation of M. This does not have other implications than a small variation of M of the pristine material.

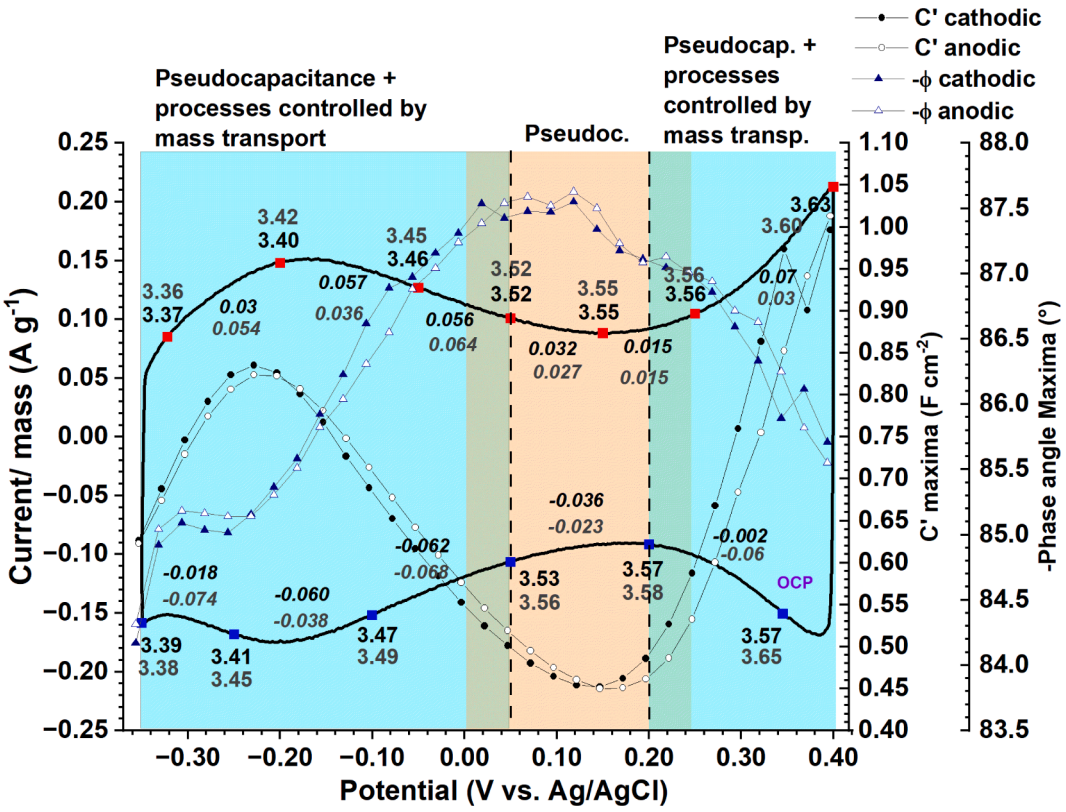

Fig. 10. A CV of the $V_4C_3T_z$ film electrode, measured *ex situ* at 0.5 mV s^{-1} scan rate, where potentials of polarization in reduction (blue) and oxidation (red) are indicated. The oxidation states determined by XAS are shown at the exterior of the CV next to the corresponding polarization potential. The changes in oxidation state are shown at the interior of the CV and in between the potentials of polarization. Black font indicates cycle 1 and gray font indicates cycle 2. Capacitance C' and -Phase angle vs. potential curves, as determined by EIS, are plotted. Potential regions where particular charge storage mechanisms predominate (pseudocapacitance or pseudocapacitance plus processes controlled by mass transport) are indicated in color. EDLC has a contribution over the entire electrochemical window.

Table 2
Charge and capacitance per unit mass calculated according to the oxidation-reduction processes reported by the *in situ* XAS measurements over a 0.4 V to − 0.35 V vs. Ag/AgCl electrochemical window. Reduction (R) and oxidation (O) over two cycles is reported. The electrochemical window for the first cycle was from OCP = 0.345 V to − 0.35 V vs. Ag/AgCl.

R/O-cycle	δ_i	ΔV (V)	M (g mol^{-1})	ΔQ/mass (C g^{-1})	ΔC/mass (F g^{-1})
OCP	–	-	279.82	–	–
R-1	− 0.1755	0.695	279.99	241.9	348.0
O-1	+0.2432	0.75	279.75	335.6	447.5
R-2	− 0.2555	0.75	280.00	352.2	469.6
O-2	+0.2215	0.75	279.78	305.6	407.5

The charge and capacitance stored over the full operational electrochemical window were calculated considering the following reduction/oxidation process [14]:

$$V_4^{n+}C_3O_x^{2-}(OH^-)_yF_{z1}Cl_{z2} + \delta e^- + \delta H^+ \rightleftharpoons V_4^{[n+\ -(\delta/4)]}C_3O_{x-\delta}^{2-}(OH^-)_{y+\delta}F_{z1}Cl_{z2} \quad (12)$$

where δ electrons are involved in the overall reduction/oxidation process. Here, the $\delta/4 = \delta_i$ (Eq. (11)) electrons involved in the reduction/oxidation process of 1 V atom are explicitly stated. The chemical groups -O and -OH and, thus M, vary according to this process. Table 2 summarizes the calculations.

Here, the net transferred charge upon oxidation-reduction processes over the full electrochemical window (O-1,R-2,O-2) reflect a very slight irreversibility. According to Eq. (12), this led to slight variations of M.

The maximum charge and capacitance stored per unit mass according to CV are 202.4 C g^{-1} and 269.8 F g^{-1} at 1 mV s^{-1}, respectively. This is lower than the quantities determined by XAS (Table 2). This is explained by the different electrochemical methods used to measure charge storage. In a CV, acquired at 1 mV s^{-1}, storage takes place for 12.5 min over an entire 0.75 V electrochemical window. In contrast, in the potentiostatic step used for the *in situ* XAS measurements, the storage took place over 15 min per polarization potential (Figure S10). During the CV the currents are "smeared out" over the entire electrochemical window [49], whereas in a potentiostatic step currents are driven at a single potential for a much longer time than in CVs [49]. This allows charge collection from the slowest diffusion-controlled processes, generally, resulting in a higher charge measured by potentiostatic steps than when using the CV method [49]. A calculation of charge stored during the potentiostatic steps at − 0.35 V and 0.4 V, i.e. by integration of the chronoamperograms (Figure S10), rendered 228.13 C g^{-1} (R-1), 348.8 C g^{-1} (0-1), 224.6 C g^{-1} (R-2) and 325.5 C g^{-1} (O-2), which are on the same range than the values calculated by the changes in oxidation states measured by XAS (Table 2). This confirms the correctness of the XAS measurements and analysis.

Next, we discuss the overall charge storage processes described in Eqs. (1) and (12). In these electrochemical mechanisms, the presence of -O groups and proton transfer are key for oxidation/reduction of the transition metal. Previous studies on $Ti_3C_2T_z$ tested in acidic electrolytes have provided evidence of the protonation of -O groups under negative polarization by a combination of UV-*vis* and Raman spectroscopies [43]. However, the deprotonation during the corresponding reverse positive polarization was not confirmed. Other studies of $Ti_3C_2T_z$ have confirmed ion intercalation/deintercalation processes in acidic electrolytes [13,15,44]. New findings on the chemistry of MXenes may be game changing on

the definition of electrochemical processes. Recently, it has been found that oxygen atoms substitute carbon atoms in MAX and MXenes [69], which surely influences charge distribution and reactivity. Here, XAS studies confirmed the reversibility of reduction/oxidation processes over the entire operational potential window. Further studies will be necessary to establish and quantify protonation/deprotonation processes as well as to establish the dynamics of proton/water (de)intercalation processes.

An interesting point of discussion is that the changes in oxidation state here found are much higher (Table 2, column 2) than for the case of $Ti_3C_2T_z$, where only a 0.1 electron transfer was reported over a 0.7 V electrochemical window tested in 1 M H_2SO_4 [12]. This indicates a superior redox activity of this V-based MXene over Ti-based MXenes. Although the determined capacitance by CV methods of 269.8 F g^{-1} for $V_4C_3T_z$ is only slightly larger than 245 F g^{-1} for $Ti_3C_2T_z$, the XAS results revealed a much larger attainable capacitance of up to 469.6 F g^{-1} (Table 2). Notice that here the electrodes were used as vacuum-filtrated films, where ion transport across the films is not optimized. Enhanced charge storage in $Ti_3C_2T_z$ film electrodes has been achieved by introducing hydrogels in between the nanosheets or nanosheet porosity [14]. This has resulted in a up to 2-fold increase in capacitance [14]. A similar optimization of $V_4C_3T_z$ electrodes should lead to similar or higher increase of capacitance measured by CV, as predicted by XAS.

4. Conclusions

Synthesized $V_4C_3T_z$ consisted of monolayer/few-layers material. High-end microscopy confirmed the presence of monolayer material and revealed details of its atomic structure. A crystal consisting of a 4:3 V:C stoichiometry was confirmed with the presence of vacancies and pores highly desirable to facilitate ion transport processes across nanosheets. Elemental studies confirmed the elemental composition of the MXene and surface chemical groups. Rietveld refinement informed of the hexagonal crystal structure of V_4AlC_3 and key structural parameters. Analysis of XRD data of etched and delaminated products enabled a correlation of XRD pattern features with key 3D to 2D crystal structure transformations occurring upon etching and delamination. This has important implications in guiding the synthesis of fully delaminated MXenes.

$V_4C_3T_z$ film electrodes showed excellent charge storage properties in 3 M H_2SO_4 and in a 0.75 V electrochemical window. A capacity and capacitance of 202.4 C g^{-1}/0.52 C cm^{-2}/ 647.8 C cm^{-3} and 269.8 F g^{-1}/ 0.67 F cm^{-2}/863.7 F cm^{-3} were achieved -as measured by CV. Even a higher storage (469.6 F g^{-1}) was reported by *in situ* XAS measurements and potentiostatic steps. A number of up to $\delta_i = 0.25$ electrons per V atom (Table 2) were exchanged during reduction/oxidation processes over a 0.75 V electrochemical window, which was superior to 0.1 electrons per Ti atom exchanged in $Ti_3C_2T_z$ over a 0.7 V electrochemical window in 1 M H_2SO_4 [12]. This demonstrated the superior performance of this 4:3 V-based MXene over such Ti-based 3:2 MXene.

An excellent rate performance was achieved with 62.8 % of capacitance retention at 100 mV s^{-1} (as measured by CV) and a storage of 100 C g^{-1} at the very high GCPL rate of 30 A g^{-1}. The electrode showed and excellent cycling stability demonstrated up to 10,000 cycles. The high stability of $V_4C_3T_z$ in the highly acidic 3 M H_2SO_4 electrolyte must be highlighted. Generally, MXenes show a superior charge storage in acidic than in neutral electrolytes, due to the comparatively higher ionic conductivity of the former. In order to exploit this high charge storage capacity, the MXene must be stable in such highly acidic electrolyte. Here, $V_4C_3T_z$ complied with this prerequisite, showing excellent stability. MXenes with other chemical composition may or may not be stable in highly acidic electrolytes, such as (Mo,V) 4:3 mixed MXenes, which have been preferably tested in neutral to slightly acidified electrolytes [27]. A $V_4C_3T_z$/Carbon full cell was tested as a proof of concept, which achieved maximum energy and power per unit mass of of 14.7 Wh kg^{-1} and power of 9.74 kW kg^{-1}, respectively; and maximum energy and power per unit volume of 10.5 mWh cm^{-3} and 7.0 W cm^{-3}, respectively.

Charge storage mechanisms were investigated combining three key methods: *in situ* XAS, evaluation of the charge storage-controlling mechanisms (electrochemical kinetics or mass transport) via the application of models 1 and 2, and SPEIS. *In situ*XAS allowed to identify and quantify redox activity over the full working electrochemical window. Insights from the three methods allowed to establish the predominance of charge storage mechanisms at defined potential regions. The predominant mechanisms were pseudocapacitance or pseudocapacitance plus a minor contribution of processes controlled by mass transport, having transition regions in between. In addition, EDLC processes had a minor contribution over the entire electrochemical window.

$V_4C_3T_z$ film electrodes showed an excellent chemical stability in standard atmospheres, which together with their flexibility, high electrical conductivity (free standing electrodes) and high volumetric capacitance make up for an excellent candidate for applications where miniaturized compact energy storage devices are required such as micro-/wearable electronics.

CRediT authorship contribution statement

Beatriz Mendoza-Sánchez (First and Senior author): Conceptualization, Methodology, Software, Validation, Formal analysis, Investigation, Resources, Data curation, Writing – original draft, Writing – review & editing, Visualization, Supervision, Project administration, Resources, Funding acquisition. **Atharva H. Ladole:** Investigation. **Enrique Samperio-Niembro:** Investigation, Visualization. **Stefan Mangold:** Investigation, Formal analysis. **Michael Knapp:** Formal analysis, Resources, Funding acquisition. **Eric N. Tseng:** Investigation, Formal analysis. **Per O.Å. Persson:** Formal analysis. **Camille Douard:** Investigation. **Christopher E. Shuck:** Investigation, Writing – review & editing. **Thierry Brousse:** Formal analysis, Writing – review & editing.

Declaration of competing interest

The authors declare that they have no known competing financial interests or personal relationships that could have appeared to influence the work reported in this paper.

Acknowledgements

B.M.-S. acknowledges the Helmholtz Association for a Helmholtz ERC Recognition Award (ERC-RA-0028). Yury Gogotsi (Drexel University) is acknowledged for his kind gesture providing MAX materials. This work contributes to the research performed at the Centre for Electrochemical Energy Storage Ulm-Karlsruhe (CELEST). C.D. and T.B. acknowledge Labex STORE-EX (ANR-10-LABX-7601) for financial support.

The Knut and Alice Wallenberg Foundation is acknowledged for support of the electron microscopy laboratory in Linköping. The Swedish Research Council and the Swedish Foundation for Strategic Research is acknowledged for access to ARTEMI, the Swedish National Infrastructure in Advanced Electron Microscopy (Grants No. 2021-00171 and RIF21-0026)

Supplementary material

Supplementary material associated with this article can be found, in the online version, at 10.1016/j.ensm.2024.103566

References

[1] B. Anasori, M.R. Lukatskaya, Y. Gogotsi, 2D metal carbides and nitrides (MXenes) for energy storage, Nat. Rev. Mater. 2 (2) (2017) 16098, https://doi.org/10.1038/natrevmats.2016.98.

[2] A. VahidMohammadi, J. Rosen, Y. Gogotsi, The world of two-dimensional carbides and nitrides (MXenes), Science 372 (6547) (2021) eabf1581.https://www.science.org/doi/abs/10.1126/science.abf1581

[3] M. Han, K. Maleski, C.E. Shuck, Y. Yang, J.T. Glazar, A.C. Foucher, K. Hantanasirisakul, A. Sarycheva, N.C. Frey, S.J. May, V.B. Shenoy, E.A. Stach, Y. Gogotsi, Tailoring electronic and optical properties of MXenes through forming solid solutions, J. Am. Chem. Soc. 142 (45) (2020) 19110–19118, https://doi.org/10.1021/jacs.0c07395.

[4] W. Hong, B.C. Wyatt, S.K. Nemani, B. Anasori, Double transition-metal MXenes: atomistic design of two-dimensional carbides and nitrides - ADDENDUM, MRS Bull. (2020).1-1

[5] Y. Gogotsi, B. Anasori, The rise of MXenes, ACS Nano 13 (8) (2019) 8491–8494. https://www.ncbi.nlm.nih.gov/pubmed/31454866

[6] B. Mendoza-Sánchez, Y. Gogotsi, Synthesis of two-dimensional materials for capacitive energy storage, Adv. Mater. 28 (29) (2016) 6104–6135, https://doi.org/10.1002/adma.201506133.

[7] M. Naguib, J. Come, B. Dyatkin, V. Presser, P.-L. Taberna, P. Simon, M. W. Barsoum, Y. Gogotsi, MXene: a promising transition metal carbide anode for lithium-ion batteries, Electrochem. Commun. 16 (1) (2012) 61–64.https://www.sciencedirect.com/science/article/pii/S1388248112000070

[8] A. VahidMohammadi, A. Hadjikhani, S. Shahbazmohamadi, M. Beidaghi, Two-dimensional vanadium carbide (MXene) as a high-capacity cathode material for rechargeable aluminum batteries, ACS Nano 11 (11) (2017) 11135–11144, https://doi.org/10.1021/acsnano.7b05350.

[9] S.-M. Bak, R. Qiao, W. Yang, S. Lee, X. Yu, B. Anasori, H. Lee, Y. Gogotsi, X.-Q. Yang, Na-Ion intercalation and charge storage mechanism in 2D vanadium carbide, Adv. Energy Mater. 7 (20) (2017) 1700959, https://doi.org/10.1002/aenm.201700959.

[10] X. Tang, X. Guo, W. Wu, G. Wang, 2D metal carbides and nitrides (MXenes) as high-performance electrode materials for lithium-based batteries, Adv. Energy Mater. 8 (33) (2018) 1801897, https://doi.org/10.1002/aenm.201801897.

[11] M. Okubo, A. Sugahara, S. Kajiyama, A. Yamada, MXene as a charge storage host, Accounts Chem. Res. 51 (3) (2018) 591–599, https://doi.org/10.1021/acs.accounts.7b00481.

[12] M.R. Lukatskaya, S.-M. Bak, X. Yu, X.-Q. Yang, M.W. Barsoum, Y. Gogotsi, Probing the mechanism of high capacitance in 2D titanium carbide using in situ X-ray absorption spectroscopy, Adv. Energy Mater. 5 (15) (2015) 1500589, https://doi.org/10.1002/aenm.201500589.

[13] M.D. Levi, M.R. Lukatskaya, S. Sigalov, M. Beidaghi, N. Shpigel, L. Daikhin, D. Aurbach, M.W. Barsoum, Y. Gogotsi, Solving the capacitive paradox of 2D MXene using electrochemical quartz-crystal admittance and in situ electronic conductance measurements, Adv. Energy Mater. 5 (1) (2015) 1400815.10.1002/aenm.201400815

[14] M.R. Lukatskaya, S. Kota, Z. Lin, M.-Q. Zhao, N. Shpigel, M.D. Levi, J. Halim, P.-L. Taberna, M.W. Barsoum, P. Simon, Y. Gogotsi, Ultra-high-rate pseudocapacitive energy storage in two-dimensional transition metal carbides, Nat. Energy 2 (8) (2017) 17105, https://doi.org/10.1038/nenergy.2017.105.

[15] X. Mu, D. Wang, F. Du, G. Chen, C. Wang, Y. Wei, Y. Gogotsi, Y. Gao, Y. Dall'Agnese, Revealing the pseudo-intercalation charge storage mechanism of MXenes in acidic electrolyte, Adv. Funct. Mater. 29 (29) (2019) 1902953, https://doi.org/10.1002/adfm.201902953.

[16] M.R. Lukatskaya, O. Mashtalir, C.E. Ren, Y. Dall'Agnese, P. Rozier, P.L. Taberna, M. Naguib, P. Simon, M.W. Barsoum, Y. Gogotsi, Cation intercalation and high volumetric capacitance of two-dimensional titanium carbide, Science 341 (6153) (2013) 1502–1505.http://www.ncbi.nlm.nih.gov/pubmed/24072919

[17] X. Wang, T.S. Mathis, K. Li, Z. Lin, L. Vlcek, T. Torita, N.C. Osti, C. Hatter, P. Urbankowski, A. Sarycheva, M. Tyagi, E. Mamontov, P. Simon, Y. Gogotsi, Influences from solvents on charge storage in titanium carbide MXenes, Nat. Energy 4 (3) (2019) 241–248, https://doi.org/10.1038/s41560-019-0339-9.

[18] M. Han, C.E. Shuck, R. Rakhmanov, D. Parchment, B. Anasori, C.M. Koo, G. Friedman, Y. Gogotsi, Beyond $Ti_3C_2T_x$: MXenes for electromagnetic interference shielding, ACS Nano 14 (4) (2020) 5008–5016, https://doi.org/10.1021/acsnano.0c01312.

[19] Q. Yang, Y. Wang, X. Li, H. Li, Z. Wang, Z. Tang, L. Ma, F. Mo, C. Zhi, Recent progress of MXene-based nanomaterials in flexible energy storage and electronic devices, Energy Environ. Mater. 1 (4) (2018) 183–195, https://doi.org/10.1002/eem2.12023.

[20] X. Wang, S. Kajiyama, H. Iinuma, E. Hosono, S. Oro, I. Moriguchi, M. Okubo, A. Yamada, Pseudocapacitance of MXene nanosheets for high-power sodium-ion hybrid capacitors, Nat. Commun. 6 (1) (2015) 6544, https://doi.org/10.1038/ncomms7544.

[21] Y. Yoon, M. Lee, S.K. Kim, G. Bae, W. Song, S. Myung, J. Lim, S.S. Lee, T. Zyung, K.-S. An, A strategy for synthesis of carbon nitride induced chemically doped 2D MXene for high-performance supercapacitor electrodes, Adv. Energy Mater. 8 (15) (2018) 1703173, https://doi.org/10.1002/aenm.201703173.

[22] J. Halim, S. Kota, M.R. Lukatskaya, M. Naguib, M.-Q. Zhao, E.J. Moon, J. Pitock, J. Nanda, S.J. May, Y. Gogotsi, M.W. Barsoum, Synthesis and characterization of 2D molybdenum carbide (MXene), Adv. Funct. Mater. 26 (18) (2016) 3118–3127, https://doi.org/10.1002/adfm.201505328.

[23] Q. Tao, M. Dahlqvist, J. Lu, S. Kota, R. Meshkian, J. Halim, J. Palisaitis, L. Hultman, M.W. Barsoum, P.O.Å. Persson, J. Rosen, Two-dimensional $Mo_{1.33}C$ MXene with divacancy ordering prepared from parent 3D laminate with in-plane chemical ordering, Nat. Commun. 8 (1) (2017) 14949, https://doi.org/10.1038/ncomms14949.

[24] Q. Shan, X. Mu, M. Alhabeb, C.E. Shuck, D. Pang, X. Zhao, X.-F. Chu, Y. Wei, F. Du, G. Chen, Y. Gogotsi, Y. Gao, Y. Dall'Agnese, Two-dimensional vanadium carbide (V_2C) MXene as electrode for supercapacitors with aqueous electrolytes, Electrochem. Commun. 96 (2018) 103–107.https://www.sciencedirect.com/science/article/pii/S1388248118302650

[25] Y. DallAgnese, P.-L. Taberna, Y. Gogotsi, P. Simon, Two-dimensional vanadium carbide (MXene) as positive electrode for sodium-ion capacitors, J. Phys. Chem. Lett. 6 (12) (2015) 2305–2309, https://doi.org/10.1021/acs.jpclett.5b00868.

[26] B. Anasori, Y. Xie, M. Beidaghi, J. Lu, B.C. Hosler, L. Hultman, P.R.C. Kent, Y. Gogotsi, M.W. Barsoum, Two-dimensional, ordered, double transition metals carbides (MXenes), ACS Nano 9 (10) (2015) 9507–9516, https://doi.org/10.1021/acsnano.5b03591.

[27] D. Pinto, B. Anasori, H. Avireddy, C.E. Shuck, K. Hantanasirisakul, G. Deysher, J. R. Morante, W. Porzio, H.N. Alshareef, Y. Gogotsi, Synthesis and electrochemical properties of 2D molybdenum vanadium carbides - solid solution MXenes, J. Mater. Chem. A 8 (18) (2020) 8957–8968, https://doi.org/10.1039/D0TA01798A.

[28] K. Matthews, T. Zhang, C.E. Shuck, A. VahidMohammadi, Y. Gogotsi, Guidelines for synthesis and processing of chemically stable two-dimensional V_2CT_x MXene, J. Mater. Chem. 34 (2) (2022) 499–509, https://doi.org/10.1021/acs.chemmater.1c03508.

[29] C. Hu, J. Zhang, J. Wang, F. Li, J. Wang, Y. Zhou, Crystal structure of V_4AlC_3: a new layered ternary carbide, J. Am. Ceram. Soc. 91 (2) (2008) 636–639, https://doi.org/10.1111/j.1551-2916.2007.02136.x.

[30] M.H. Tran, T. Schäfer, A. Shahraei, M. Dürrschnabel, L. Molina-Luna, U.I. Kramm, C.S. Birkel, Adding a new member to the MXene family: synthesis, structure, and electrocatalytic activity for the hydrogen evolution reaction of $V_4C_3T_x$, ACS Appl. Energy Mater. 1 (8) (2018) 3908–3914, https://doi.org/10.1021/acsaem.8b00652.

[31] M. Ghidiu, M.R. Lukatskaya, M.-Q. Zhao, Y. Gogotsi, M.W. Barsoum, Conductive two-dimensional titanium carbide clay with high volumetric capacitance, Nature 516 (7529) (2014) 78–81, https://doi.org/10.1038/nature13970.

[32] O. Mashtalir, M. Naguib, V.N. Mochalin, Y. DallAgnese, M. Heon, M.W. Barsoum, Y. Gogotsi, Intercalation and delamination of layered carbides and carbonitrides, Nat. Commun. 4 (2013) 1716, https://doi.org/10.1038/ncomms2664.

[33] R. Syamsai, A.N. Grace, Synthesis, properties and performance evaluation of vanadium carbide MXene as supercapacitor electrodes, Ceram. Int. 46 (4) (2020) 5323–5330.https://www.sciencedirect.com/science/article/pii/S027288421933161X

[34] X. Wang, S. Lin, H. Tong, Y. Huang, P. Tong, B. Zhao, J. Dai, C. Liang, H. Wang, X. Zhu, Y. Sun, S. Dou, Two-dimensional V_4C_3 MXene as high performance electrode materials for supercapacitors, Electroch. Acta 307 (2019) 414–421. https://www.sciencedirect.com/science/article/pii/S0013468619306395

[35] H. Li, X. Wang, H. Li, S. Lin, B. Zhao, J. Dai, W. Song, X. Zhu, Y. Sun, Capacitance improvements of $V_4C_3T_x$ by NH_3 annealing, J. Alloys Compd. 784 (2019) 923–930. https://www.sciencedirect.com/science/article/pii/S0925838819301197

[36] M. Han, C.E. Shuck, A. Singh, Y. Yang, A.C. Foucher, A. Goad, B. McBride, S. J. May, V.B. Shenoy, E.A. Stach, Y. Gogotsi, Efficient microwave absorption with $V_{n+1}C_nT_x$ MXenes, Cell Rep. Phys. Sci 3 (10) (2022) 101073.https://www.sciencedirect.com/science/article/pii/S2666386422003678

[37] Y. Huang, J. Shen, S. Lin, W. Song, X. Zhu, Y. Sun, Defect-free few-layer M_4C_3Tx (M = V, Nb, Ta) MXene nanosheets: synthesis, characterization, and physicochemical properties, Adv. Sci. 10 (28) (2023) 2302882, https://doi.org/10.1002/advs.202302882.

[38] Y. Mao, J. Bai, S. Lin, P. Wang, W. Li, K. Xiao, S. Wang, X. Zhu, B. Zhao, Y. Sun, Two birds with one stone: V_4C_3 MXene synergistically promoted VS_2 cathode and zinc anode for high-performance aqueous zinc-ion batteries, Small 20 (11) (2024) 2306615, https://doi.org/10.1002/smll.202306615.

[39] M. Shekhirev, C.E. Shuck, A. Sarycheva, Y. Gogotsi, Characterization of MXenes at every step, from their precursors to single flakes and assembled films, Prog. Mater. Sci. 120 (2021) 100757.https://www.sciencedirect.com/science/article/pii/S0079642520301213

[40] Y. Xie, Y. Dall'Agnese, M. Naguib, Y. Gogotsi, M.W. Barsoum, H.L. Zhuang, P. R. Kent, Prediction and characterization of MXene nanosheet anodes for non-lithium-ion batteries, ACS Nano 8 (9) (2014) 9606–9615.https://www.ncbi.nlm.nih.gov/pubmed/25157692

[41] A. Yamada, J.B. Goodenough, Keggin-type heteropolyacids as electrode materials for electrochemical supercapacitors, J. Electrochem. Soc. 145 (3) (1998) 737, https://doi.org/10.1149/1.1838339.

[42] D.A. McKeown, P.L. Hagans, L.P.L. Carette, A.E. Russell, K.E. Swider, D.R. Rolison, Structure of hydrous ruthenium oxides: implications for charge storage, J. Phys. Chem. B 103 (23) (1999) 4825–4832, https://doi.org/10.1021/jp990096n.

[43] P. Salles, D. Pinto, K. Hantanasirisakul, K. Maleski, C.E. Shuck, Y. Gogotsi, Electrochromic effect in titanium carbide MXene thin films produced by dip-coating, Adv. Funct. Mater. 29 (17) (2019) 1809223, https://doi.org/10.1002/adfm.201809223.

[44] H. Shao, K. Xu, Y.-C. Wu, A. Iadecola, L. Liu, H. Ma, L. Qu, E. Raymundo-Piero, J. Zhu, Z. Lin, P.-L. Taberna, P. Simon, Unraveling the charge storage mechanism of $Ti_3C_2T_x$ MXene electrode in acidic electrolyte, ACS Energy Lett. 5 (9) (2020) 2873–2880, https://doi.org/10.1021/acsenergylett.0c01290.

[45] Y. Sun, C. Zhan, P.R.C. Kent, M. Naguib, Y. Gogotsi, D. Jiang, Proton redox and transport in MXene-confined water, ACS Appl. Mater. Interfaces. 12 (1) (2020) 763–770, https://doi.org/10.1021/acsami.9b18139.

[46] J. Rodriguez-Carvajal, FULLPROF: a program for Rietveld refinement and pattern matching analysis. Abstracts of the Satellite Meeting on Powder Diffraction of the XV Congress of the IUCr, 1990, p. 127.

[47] N. Goubard-Bretesch, O. Crosnier, C. Douard, A. Iadecola, R. Retoux, C. Payen, M.-L. Doublet, K. Kisu, E. Iwama, K. Naoi, F. Favier, T. Brousse, Unveiling pseudocapacitive charge storage behavior in $FeWO_4$ electrode material by

operando X-ray absorption spectroscopy, Small 16 (33) (2020) 2002855, https://doi.org/10.1002/smll.202002855.
[48] J.C. Espinosa-Angeles, E. Quarez, L.-B. Mvele Eya, C. Douard, A. Iadecola, H. Shao, P.-L. Taberna, P. Simon, O. Crosnier, T. Brousse, Charge storage mechanism of Li_xWO_3 hexagonal tungsten bronze in aqueous electrolytes, Batteries 9 (2) (2023). https://www.mdpi.com/2313-0105/9/2/136
[49] M.F. Dupont, S.W. Donne, Separating the faradaic and non-faradaic contributions to the total capacitance for different manganese dioxide phases, J. Electrochem. Soc. 162 (5) (2015) A5096, https://doi.org/10.1149/2.0161505jes.
[50] J.S. Ko, C.-H. Lai, J.W. Long, D.R. Rolison, B. Dunn, J. Nelson Weker, Differentiating double-layer, pseudocapacitance, and battery-like mechanisms by analyzing impedance measurements in three dimensions, ACS Appl. Mater. Interfaces. 12 (12) (2020) 14071–14078, https://doi.org/10.1021/acsami.0c02020.
[51] N. Kurra, S. Uzun, G. Valurouthu, Y. Gogotsi, Mapping (Pseudo) capacitive charge storage dynamics in titanium carbide MXene electrodes in aqueous electrolytes using 3D bode analysis, Energy Storage Mater. 39 (2021) 347–353.https://www.sciencedirect.com/science/article/pii/S2405829721001860
[52] P.L. Taberna, P. Simon, J.F. Fauvarque, Electrochemical Characteristics and impedance spectroscopy studies of carbon-carbon supercapacitors, J. Electrochem. Soc. 150 (3) (2003) A292–A300.http://jes.ecsdl.org/content/150/3/A292.abstract
[53] B. Mendoza-Snchez, E. Samperio-Niembro, O. Dolotko, T. Bergfeldt, C. Kbel, M. Knapp, C.E. Shuck, Systematic study of the multiple variables involved in V_2AlC acid-based etching processes, a key step in MXene synthesis, ACS Appl. Mater. Interfaces. 15 (23) (2023) 28332–28348, https://doi.org/10.1021/acsami.3c01671.
[54] J. Coelho, B. Mendoza-Snchez, H. Pettersson, A. Pokle, E.K. McGuire, E. Long, L. McKeon, A. P. Bell, V. Nicolosi, Manganese oxide nanosheets and a 2D hybrid of graphene-manganese oxide nanosheets synthesized by liquid-phase exfoliation, 2D Mater. 2 (2) (2015) 025005.http://stacks.iop.org/2053-1583/2/i=2/a=025005
[55] A. Gloter, V. Serin, C. Turquat, C. Cesari, C. Leroux, G. Nihoul, Vanadium valency and hybridization in V-doped hafnia investigated by electron energy loss spectroscopy, Eur. Phys. J. B (EPJ B) 22 (2) (2001) 179–186, https://doi.org/10.1007/PL00011142.
[56] K.S. Liang, R.R. Chianelli, F.Z. Chien, S.C. Moss, Structure of poorly crystalline MoS_2 - a modeling study, J.. Non-Cryst. Solids 79 (3) (1986) 251–273.https://www.sciencedirect.com/science/article/pii/0022309386902267
[57] M. Ghidiu, M.W. Barsoum, The 110 reflection in X-ray diffraction of MXene films: misinterpretation and measurement via non-standard orientation, J. Am. Ceram. Soc. 100 (12) (2017) 5395–5399.
[58] R. Compton, C. Banks, Understanding Voltammetry, World Scientific Publishing Co. Pte. Ltd., Oxford, UK, 2007.
[59] H. Shao, Z. Lin, K. Xu, P.-L. Taberna, P. Simon, Electrochemical study of pseudocapacitive behavior of $Ti_3C_2T_x$ MXene material in aqueous electrolytes, Energy Storage Mater. 18 (2019) 456–461.
[60] A. VahidMohammadi, M. Mojtabavi, N.M. Caffrey, M. Wanunu, M. Beidaghi, Assembling 2D MXenes into highly stable pseudocapacitive electrodes with high power and energy densities, Adv. Mater. 31 (8) (2019) 1806931, https://doi.org/10.1002/adma.201806931.
[61] S. Zhao, C. Chen, X. Zhao, X. Chu, F. Du, G. Chen, Y. Gogotsi, Y. Gao, Y. Dall'Agnese, Flexible $Nb_4C_3T_x$ film with large interlayer spacing for high-performance supercapacitors, Adv. Funct. Mater. 30 (47) (2020) 2000815, https://doi.org/10.1002/adfm.202000815.
[62] H. Avireddy, B.W. Byles, D. Pinto, J.M. Delgado Galindo, J.J. Biendicho, X. Wang, C. Flox, O. Crosnier, T. Brousse, E. Pomerantseva, J.R. Morante, Y. Gogotsi, Stable high-voltage aqueous pseudocapacitive energy storage device with slow self-discharge, Nano Energy 64 (2019) 103961.https://www.sciencedirect.com/science/article/pii/S2211285519306688
[63] T.-C. Liu, W.G. Pell, B.E. Conway, S.L. Roberson, Behavior of Molybdenum nitrides as materials for electrochemical capacitors: comparison with ruthenium oxide, J. Electrochem. Soc. 145 (6) (1998) 1882, https://doi.org/10.1149/1.1838571.
[64] A.J. Bard, F. L, Electrochemical Methods: Fundamentals and Applications, second ed., John Wiley & Sons, Inc, Unites States of America, 2001.
[65] W. van den Bergh, M. Stefik, Understanding rapid intercalation materials one parameter at a time, Adv. Funct. Mater. 32 (31) (2022) 2204126, https://doi.org/10.1002/adfm.202204126.
[66] J.R. Miller, R.A. Outlaw, B.C. Holloway, Graphene double-layer capacitor with ac line-filtering performance, Science 329 (5999) (2010) 1637–1639.http://www.sciencemag.org/content/329/5999/1637.abstract
[67] M.A. Hope, A.C. Forse, K.J. Griffith, M.R. Lukatskaya, M. Ghidiu, Y. Gogotsi, C. P. Grey, NMR reveals the surface functionalisation of Ti_3C_2 MXene, PCCP 18 (7) (2016) 5099–5102, https://doi.org/10.1039/C6CP00330C.
[68] K.J. Harris, M. Bugnet, M. Naguib, M.W. Barsoum, G.R. Goward, Direct measurement of surface termination groups and their connectivity in the 2D MXene V_2CT_x using NMR spectroscopy, J. Phys. Chem. C 119 (24) (2015) 13713–13720, https://doi.org/10.1021/acs.jpcc.5b03038.
[69] P.P. Michałowski, M. Anayee, T.S. Mathis, S. Kozdra, A. Wjcik, K. Hantanasirisakul, I. Jóźwik, A. Piątkowska, M. Mozdzonek, A. Malinowska, R. Diduszko, E. Wierzbicka, Y. Gogotsi, Oxycarbide MXenes and MAX phases identification using monoatomic layer-by-layer analysis with ultralow-energy secondary-ion mass spectrometry, Nat. Nanotechnol. 17 (11) (2022) 1192–1197, https://doi.org/10.1038/s41565-022-01214-0.